Materials Science & Engineering A 871 (2023) 144910

Contents lists available at ScienceDirect

Materials Science & Engineering A

journal homepage: www.elsevier.com/locate/msea

Improved microstructure, mechanical properties and electrical conductivity of the Cu–Ni–Sn–Ti–Cr alloy due to Ce micro-addition

Shunlong Tang [a], Meng Zhou [a,b,c,**], Yi Zhang [a,b,c,*], Deye Xu [a], Zhiyang Zhang [a], Xianhua Zheng [a], De Li [a], Xu Li [d], Baohong Tian [a,b,c], Yanlin Jia [e], Yong Liu [a,b,c], Alex A. Volinsky [f,g], Ekaterina S. Marchenko [g]

[a] Henan University of Science and Technology, School of Materials Science and Engineering, Luoyang, 471023, PR China
[b] Provincial and Ministerial Co-construction of Collaborative Innovation Center for Non-ferrous Metals New Materials and Advanced Processing Technology, Henan Province, Luoyang, 471023, PR China
[c] Henan Province Key Laboratory of Nonferrous Materials Science and Processing Technology, Luoyang, 471023, PR China
[d] National Institute of Metrology, Center for Advanced Measurement Science, Beijing, 100029, PR China
[e] Central South University, College of Materials Science and Engineering, Changsha, 410083, PR China
[f] University of South Florida, Department of Mechanical Engineering, 4202 E. Fowler Ave. ENG 030, Tampa, 33620, USA
[g] Laboratory of Superelastic Biointerfaces, National Research Tomsk State University, 36 Lenin Ave, 634045, Tomsk, Russia

ARTICLE INFO

Keywords:
Copper alloys
Mechanical properties
EBSD
Microstructure
Strengthening and conductivity mechanisms

ABSTRACT

In this paper, new Cu–Ni–Sn–Ti–Cr and Cu–Ni–Sn–Ti–Cr–Ce alloys were prepared and studied. After solution treatment and 60% cold rolling, the Cu–Ni–Sn–Ti–Cr alloy with micro-hardness of 221 HV, a tensile strength of 598.1 MPa, elongation of 9.9% and electrical conductivity of 45.2% IACS was obtained after aging at 500 °C for 60 min. Furthermore, the new Cu–Ni–Sn–Ti–Cr–Ce alloy was also obtained using aging at 500 °C for 60 min, having 245 HV micro-hardness, 645.2 MPa tensile strength, elongation 9.4% and 44.6% IACS conductivity. The comprehensive properties of high strength, hardness, and electrical conductivity of the alloy are attributed to the composite effects of solution, deformation, grain boundary, and precipitation strengthening. Among them, precipitation strengthening plays a major role, and the precipitates are mainly nanometer $CuNi_2Ti$, Cr, and NiTi phases. The interface between the nanometer $CuNi_2Ti$ phase and Cu matrix is a coherent, which can improve the strength of the alloy without sacrificing plasticity. In addition, texture type transformation and texture strength change of the alloy are closely related to the increase of micro-hardness. The micro-addition of trace rare earth Ce can refine the alloy grains, and promote dynamic recrystallization to produce finer grains, significantly improving the alloy's micro-hardness.

1. Introduction

Various copper alloys with different properties can be formed by adding other elements to copper. In general, the comprehensive properties of copper alloys are better compared with pure copper. Copper alloys with excellent properties are widely used in communications, transportation, high-voltage electrical appliances, and other fields [1–5]. With the rapid development of electronic power devices and mobile phone equipment, the demand for copper alloys and other metals with high strength, electrical conductivity, and stability is increasing. Although Cu–Be alloy's strength, electrical conductivity, and other comprehensive properties are adequate, the Cu–Be alloy is toxic and very harmful to human health, so it is necessary to find a non-toxic alloy to replace it. Cu-Ni-Sn [6,7], Cu-Ti [8,9], Cu-Fe-Ti [10,11], Cu-Al-Ni [12,13], Cu–Cr–Nb alloys [14,15], and others have been used as potential substitutes for Cu–Be alloys. In particular, Cu–Ni–Sn alloy has attracted much attention because of its excellent mechanical properties and good electrical conductivity. In the Cu–Ni–Sn alloy, Sn can improve the ability of the copper to hinder dislocation and grain movement, while Ni easily forms precipitates with Sn and Cu, which can improve the strength and electrical conductivity of copper alloys. Ni and Sn improve the strength of the Cu–Ni–Sn alloy and are non-toxic, so it is a

* Corresponding author. Henan University of Science and Technology, School of Materials Science and Engineering, Luoyang, 471023, PR China.
** Corresponding author. Henan University of Science and Technology, School of Materials Science and Engineering, Luoyang, 471023, PR China.
E-mail addresses: zhoumeng0902@126.com (M. Zhou), zhshgu436@163.com (Y. Zhang).

https://doi.org/10.1016/j.msea.2023.144910
Received 14 November 2022; Received in revised form 21 February 2023; Accepted 10 March 2023
Available online 11 March 2023

potentially environmentally friendly elastic conductive material [16].

Adding trace alloying elements into the copper matrix is an effective way to improve the strength and hardness of Cu alloys since they will form precipitates with the copper matrix or between the alloying elements. On the one hand, the precipitates strengthen the copper matrix, on the other hand, they hinder the dislocation and grain movement and improve the strength and hardness of the alloy [17]. Cheng et al. [18] found that Cu–15Ni–8Sn-0.8Nb alloy was mainly strengthened through the precipitation of $NbNi_3$ and $NbNi_2Sn$ phases at the nano-scale. Guo et al. [19] investigated the influence of discontinuous precipitation growth kinetics after adding Co to the Cu–15Ni–8Sn alloy and showed that adding Co could greatly inhibit the formation of discontinuous precipitation (DP) in the Cu–15Ni–8Sn alloy. Huang et al. [20] showed that adding Ti could promote the precipitation of nano-scale Cr precipitates in the aging treatment of Cu–Cr–Ti alloy and improve its strength. Si et al. [22] used the composite aging process to obtain the excellent comprehensive performance of the Cu-2.7Ti-0.15Mg-0.1Ce-0.1Zr alloy with 340 HV hardness, 1035 MPa tensile strength, and 20.1% IACS electrical conductivity. Besides the addition of trace alloying elements, different aging processes and aging parameters have important effects on the properties of copper alloys. Therefore, adding different trace alloying elements and optimizing aging parameters improve the properties of copper alloys.

In previous work, the microstructure and hot deformation behavior of the Cu–1Ni-0.9Sn-0.5Ti-0.3Cr alloy using the Gleeble-1500 simulator were investigated [23]. To understand the optimal aging parameters and hardening mechanisms of Cu–Ni–Sn–Ti–Cr-(Ce) alloy during aging, the mechanical properties, electrical conductivity, and microstructure evolution during aging were characterized by EBSD, TEM, HRTEM and geometric phase analysis (GPA). Moreover, the effects of Ce on the properties and microstructure evolution of the Cu–Ni–Sn–Ti–Cr alloy were also investigated.

2. Materials and methods

The raw materials for the preparation of Cu–Ni–Sn–Ti–Cr and Cu–Ni–Sn–Ti–Cr–Ce alloys included electrolytic cathode copper, pure Ni, Sn, and Cr, along with Cu–33%Ti intermediate alloy and Cu–19%Ce cut into small pieces for melting. The preparation diagram of the alloy is shown in Fig. 1. The alloy smelting was carried out in an intermediate frequency vacuum induction furnace (ZG-0.01-40-4). In addition, to the above-mentioned raw materials, a small amount of deoxidizer should be added and a certain amount of argon gas should be passed during smelting. The deoxidizer was used to remove impurities in the alloy, and argon was used to prevent oxidation. The designed and measured composition of the two alloys is listed in Table 1. The trace elements in the alloy are prone to combustion loss and the alloy ingot is prone to unbalanced solidification when cooled, so the measured components of the general alloy are slightly lower than the designed composition. The concentration of trace alloying elements in the alloy is slightly lower than designed, which may slightly lower the mechanical properties of the alloy. Therefore, for the alloying elements that can be easily lost in combustion, a larger amount can be added in the mixing process. At the same time, a certain amount of argon gas can be introduced in the melting process to prevent the trace elements in the alloy from reacting with oxygen. The molten alloy ingot (Φ90 mm × 190 mm) was placed into a Muffle furnace (YB-1600XA) for homogenization annealing at 950 °C for 4 h, and then the annealed alloy ingot was cut into 100 mm × 10 mm × 2 mm rectangular sheets. The sheets were heated to 960 °C in a vacuum OTF-1200X furnace and held for 60 min. The sample was immediately cooled in water to make the Ni, Sn, Ti, Cr, and Ce solute atoms enter the copper matrix and form an oversaturated solid solution. Then the sheet sample was cold-rolled by 60% using the three-phase asynchronous motor cold rolling machine (Y132M1-6-4 kW), which deformed and strengthened the alloy. Finally, the samples were placed into the vacuum heat treatment furnace for aging experiments at different temperatures (400–550 °C) and time (10–480 min). In order to enable the precipitation phase in the alloy to precipitate, the alloy should be aged in the two-phase zone. Therefore, according to the Cu–Ti phase diagram (Fig. 2) and previous studies on aging of copper alloys [20–22], the aging temperatures of 400 °C, 450 °C, 500 °C, and 550 °C were selected for aging. When more alloying elements such as Ni, Sn, Cr, Ti, and Ce are added to the alloy, the alloy will precipitate quickly. Therefore, a small temperature gradient is set in the early stage of aging, and a long time of 480 min is selected to make the alloy fully aged.

The properties of the alloy were tested by Sigma 2008A digital

Table 1
Composition of alloys.

Alloy	Alloy elements (wt.%)					Cu
	Ni	Sn	Ti	Cr	Ce	
Cu–1Ni-0.9Sn-0.5Ti-0.3Cr	0.912	0.862	0.411	0.269	–	Bal.
Cu–1Ni-0.9Sn-0.5Ti-0.3Cr-0.15Ce	0.886	0.837	0.424	0.254	0.108	Bal.

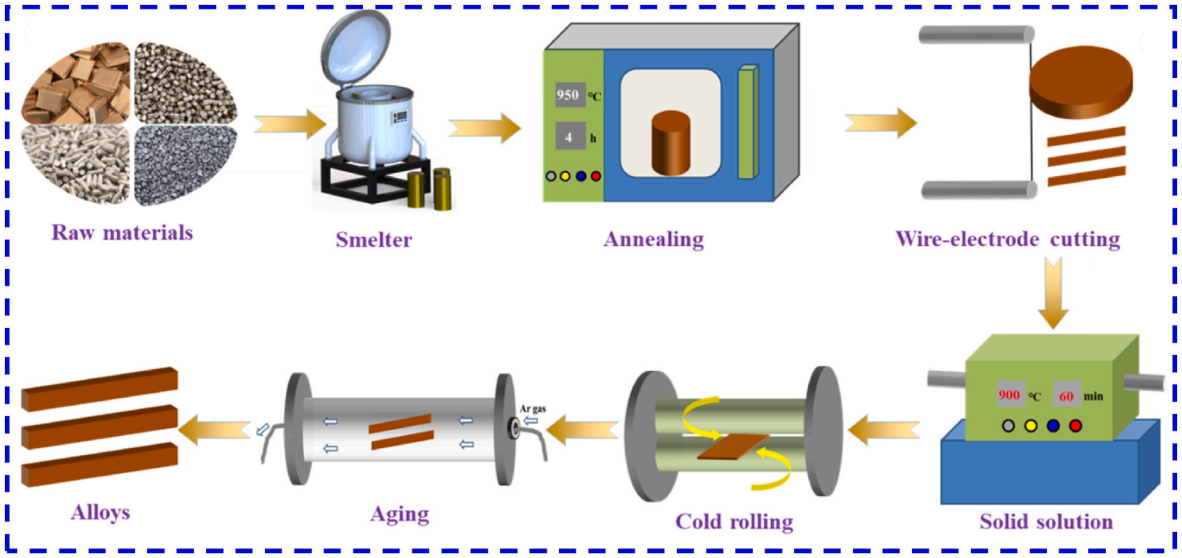

Fig. 1. Schematic diagram of the Cu–Ni–Sn–Ti–Cr and Cu–Ni–Sn–Ti–Cr–Ce alloys' preparation.

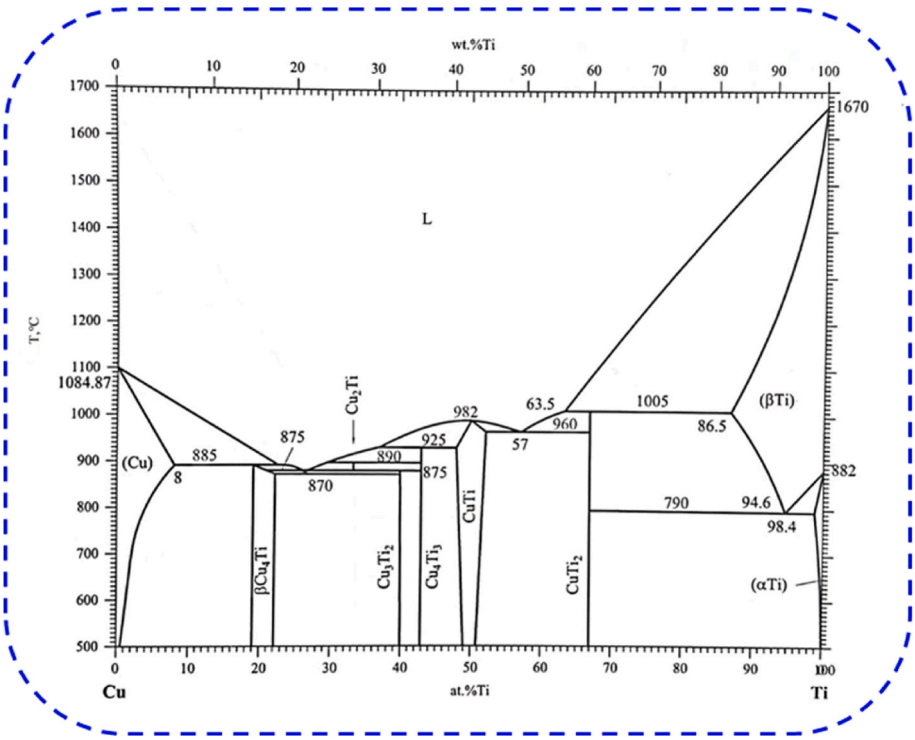

Fig. 2. Cu–Ti phase diagram [24,25].

conductivity tester, HVS-1000 hardness tester, and AG-I 250 kN machine. Each sample was measured at least five times to obtain the average electrical conductivity and reduce the experimental error. For hardness measurements, clean areas on the sample surface were indented to improve the measurement accuracy. EBSD and TEM characterization was used to obtain the microstructure of the two alloys. First, the aged sheets of Cu–Ni–Sn–Ti–Cr and Cu–Ni–Sn–Ti–Cr–Ce alloys were mechanically polished. Then the EBSD samples of the two alloys were prepared by electrolytic polishing of the thin sections in the 50% H_3PO_4 and 50% CH_3CH_2OH solution. The parameters of electrolytic polishing were 25 °C room temperature, 5 V voltage, and 1 min polishing time. The alloy sample was sanded to a 50 μm thickness and then thinned for TEM observation using Gatan 691 ion miller. The EBSD images were observed using a JSM-7800F field emission scanning electron microscope with a 0.5 μm step length and 20 kV voltage. The TEM experiments were conducted using a JSM-2100F transmission electron microscope operated at 200 kV voltage to observe the microstructure and precipitates' distribution in the alloy.

3. Results

3.1. Mechanical properties and electrical conductivity

To determine the effects of rare earth Ce on the properties of the Cu–Ni–Sn–Ti–Cr alloy after aging and to obtain the best comprehensive properties of the Cu–Ni–Sn–Ti–Cr–Ce alloy under the best aging conditions, the micro-hardness and electrical conductivity of the two kinds of alloys after aging were studied at different aging temperatures (400–550 °C) and times (10–480 min). Fig. 3 shows the mechanical properties and electrical conductivity of the Cu–Ni–Sn–Ti–Cr and Cu–Ni–Sn–Ti–Cr–Ce alloys processed at different aging temperatures and times. There are three main stages of the aging process in Fig. 3(a) and (d), namely, the under-aging, peak-aging, and over-aging [26,27]. Taking the aging at 500 °C as an example in Fig. 3(a), the micro-hardness of the alloy increased significantly with the aging time of 10–45 min, which was called the under-aging stage. The maximum micro-hardness of the alloy can reach 221 HV with the peak-aging stage between 45 min and 90 min. After 90 min aging, the micro-hardness of the alloy gradually decreased with the aging time, called the over-aging stage. The electrical conductivity of the alloy gradually increased with the aging time as seen in Fig. 3(b), which is related to the lattice distortion of the copper matrix, solute atoms, precipitated phase, and grain growth in the alloy. Fig. 3(c) shows the micro-hardness and electrical conductivity of the Cu–Ni–Sn–Ti–Cr alloy after peak-aging at different temperatures. With the aging temperature increase from 400 °C to 550 °C, the micro-hardness of the alloy first increases and then decreases, mainly because the temperature increase can provide higher energy for the solute atoms in the alloy, which is beneficial for the precipitation of solute atoms, thus improving the hardness of the alloy. However, when the temperature is too high (550 °C), the grain growth plays a leading role in phase precipitation, which softens the alloy, decreasing its hardness. The electrical conductivity of the Cu–Ni–Sn–Ti–Cr alloy in Fig. 3(c) increased with the aging temperature. The increase in aging temperature will promote grain growth and precipitation in the alloy, which will reduce the lattice distortion of the copper matrix, thereby reducing the scattering effect of electrons and increasing the electrical conductivity of the alloy.

Fig. 3(d) shows the micro-hardness of the Cu–Ni–Sn–Ti–Cr–Ce alloy after different aging temperatures and time, which has a similar trend as the Cu–Ni–Sn–Ti–Cr alloy. The micro-hardness of the alloys increased with the aging time at the under-aging stage, peaked at the peak-aging stage, and gradually decreased with the aging time at the over-aging stage. For example, in Fig. 3(d), when the aging temperature was 500 °C and the aging time was 0–480 min, the micro-hardness of Cu–Ni–Sn–Ti–Cr–Ce alloy was 146 HV, 168 HV, 189 HV, 216 HV, 245 HV, 220 HV, 196 HV, 193 HV, and 169 HV. The peak value of Cu–Ni–Sn–Ti–Cr–Ce alloy hardness is 245 HV at an aging time of 60 min. Fig. 3(e) shows the electrical conductivity of the Cu–Ni–Sn–Ti–Cr–Ce alloy at different aging temperatures and times. The electrical conductivity of the Cu–Ni–Sn–Ti–Cr–Ce alloy increased rapidly at the under-aging stage, while it increased slowly at the peak-aging and over-aging stages. As seen in Fig. 3(e), when the aging temperature was

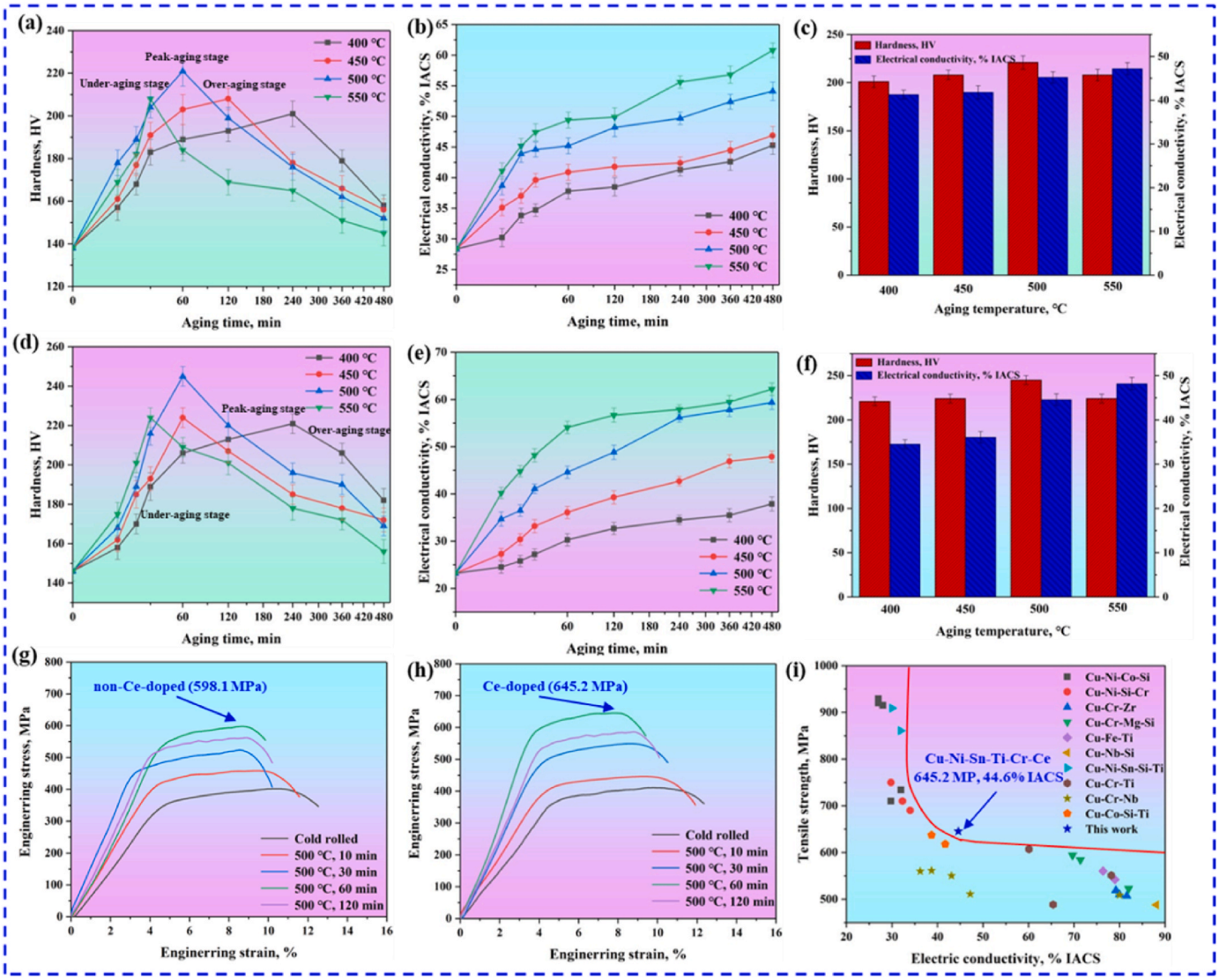

Fig. 3. Mechanical properties and electrical conductivity of Cu–Ni–Sn–Ti–Cr and Cu–Ni–Sn–Ti–Cr–Ce alloys: (a) hardness of the Cu–Ni–Sn–Ti–Cr alloy, (b) electrical conductivity of the Cu–Ni–Sn–Ti–Cr alloy, (c) hardness and conductivity of the Cu–Ni–Sn–Ti–Cr alloy during peak-aging, (d) hardness of the Cu–Ni–Sn–Ti–Cr–Ce alloy, (e) electrical conductivity of the Cu–Ni–Sn–Ti–Cr–Ce alloy, (f) Hardness and conductivity of the Cu–Ni–Sn–Ti–Cr–Ce alloy during peak-aging, (g) tensile strength of the Cu–Ni–Sn–Ti–Cr alloy under different conditions, (h) tensile strength of the Cu–Ni–Sn–Ti–Cr–Ce alloy under different conditions, (i) comparison of tensile strength vs. electrical conductivity between the presented Cu–Ni–Sn–Ti–Cr–Ce alloy and conventional copper alloys [11,27–36].

550 °C, as the aging time increased from 10 min to 480 min, the electrical conductivity was 23.2% IACS, 40.2% IACS, 44.8% IACS, 48.2% IACS, 54.1% IACS, 56.7% IACS, 57.9% IACS, 59.5% IACS and 62.2% IACS, respectively. Fig. 3(f) shows the peak-aging micro-hardness and electrical conductivity of the Cu–Ni–Sn–Ti–Cr–Ce alloy at different aging temperatures. The micro-hardness of the alloy is very sensitive to aging temperature. As the aging temperature was raised from 400 °C to 550 °C, the hardness of the alloy increased first and then decreases, from 221 HV at 400 °C to 245 HV at 500 °C, and then to 224 HV at 550 °C. The difference is that the conductivity of the alloy increases with the aging temperature. When the aging temperature was raised from 400 °C to 550 °C, the conductivity increased from 34.5% IACS to 48.2% IACS.

Tensile experiments were also carried out using the Cu–Ni–Sn–Ti–Cr and Cu–Ni–Sn–Ti–Cr–Ce alloy samples, shown in Fig. 3(g) and (h). The tensile strength of the Cu–Ni–Sn–Ti–Cr alloy after 0 min, 10 min, 30 min, 60 min, and 120 min aging time was 402.1 MPa, 458.8 MPa, 523.6 MPa, 598.1 MPa, and 562.3 MPa. The tensile strength of the Cu–Ni–Sn–Ti–Cr–Ce alloy after 0 min, 10 min, 30 min, 60 min, and 120 min aging time was 411.3 MPa, 446.3 MPa, 549.2 MPa, 645.2 MPa, and 586.2 MPa, respectively. The strength of the alloy increased first and then decreased with aging time, and was greater than after cold rolling without aging. The strength increase is consistent with the micro-hardness but contrary to the plasticity of the alloy. The tensile strength of the alloy was measured by tensile tests under different aging parameters as seen in Fig. 3(a) and (d). The strength growth trend of the alloy is consistent with the micro-hardness growth trend. The maximum micro-hardness aging temperature of 500 °C was selected for the tensile tests, and the highest tensile strength and elongation of the Cu–Ni–Sn–Ti–Cr alloy are 598.1 MPa and 9.9%, and the highest tensile strength and elongation of the Cu–Ni–Sn–Ti–Cr–Ce alloy are 645.2 MPa and 9.4%, respectively. It can be seen from Fig. 3(a) that the hardness of the Cu–Ni–Sn–Ti–Cr alloy reached the maximum value at the aging temperature of 500 °C and the aging time of 60 min, and the tensile strength of the Cu–Ni–Sn–Ti–Cr alloy reached the maximum value at the aging time of 60 min in the tensile curve in Fig. 3(g) at 500 °C. The optimal aging parameters of the Cu–Ni–Sn–Ti–Cr alloy were calculated as follows: aging temperature 500 °C and aging time 60 min, micro-hardness 221 HV, tensile strength 598.1 MPa, elongation 9.9% and

conductivity 45.2% IACS. Interestingly, the Cu–Ni–Sn–Ti–Cr–Ce alloy also had the maximum hardness at the aging temperature of 500 °C and the aging time of 60 min, as seen in Fig. 3(d), and the maximum tensile strength at the aging time of 60 min, as seen in Fig. 3(h). Finally, the optimal aging parameters of the Cu–Ni–Sn–Ti–Cr–Ce alloy were obtained, including 500 °C aging temperature and 60 min aging time, 245 HV micro-hardness, 645.2 MPa tensile strength, 9.4% elongation and 44.6% IACS electrical conductivity. Fig. 3(h) compares the tensile strength and electrical conductivity of the Cu–Ni–Sn–Ti–Cr–Ce alloy with the conventional copper alloy. The Cu–Ni–Sn–Ti–Cr–Ce alloy in the current work has good comprehensive performance.

In the aging experiment, solute atoms in the alloy have a great influence on the hardness, strength, conductivity, other properties, and microstructure of the alloy. In order to study the distribution of solute atoms in the Cu–Ni–Sn–Ti–Cr–Ce alloy, EDS experiments after solid solution strengthening and peak-aging were performed, as shown in Figs. 4 and 5. The purpose of the Cu–Ni–Sn–Ti–Cr–Ce alloy solid solution experiment was to fully dissolve Ni, Sn, Ti, Cr and Ce elements in the alloy copper matrix to form a supersaturated solid solution. As seen in Fig. 4, the trace solute elements in the Cu–Ni–Sn–Ti–Cr–Ce alloy are evenly distributed, and the at.% contents of Ni, Sn, Ti, Cr, and Ce elements are 1.6%, 1.1%, 0.3%, 0.3%, and 0.1%, respectively. It can be found by comparing Fig. 5 with Fig. 4, that the trace solute elements in the Cu–Ni–Sn–Ti–Cr–Ce alloy increased significantly, the element distribution was more uniform after aging, and the at.% contents of Ni, Sn, Ti, Cr, and Ce increased to 2.1%, 1.6%, 0.4%, 0.3%, and 0.1%, respectively. During the alloy aging, the supersaturated solid solution decomposed and the amount of solute elements precipitated in the alloy increased, which promoted the formation of precipitated phases between alloying elements and the copper matrix or between alloying elements [36]. The precipitated phase strengthens the copper matrix, hinders dislocation movement and grain movement, and increases the strength and hardness of the Cu–Ni–Sn–Ti–Cr–Ce alloy. At the same time, the precipitated phase reduces the lattice distortion of the copper matrix, which reduces the scattering effect of electrons and improves the electrical conductivity of the Cu–Ni–Sn–Ti–Cr–Ce alloy.

3.2. EBSD analysis

In order to study the microstructure and texture evolution of the Cu–Ni–Sn–Ti–Cr and Cu–Ni–Sn–Ti–Cr–Ce alloys, EBSD samples under different aging conditions were observed. Fig. 6 shows the EBSD diagram and grain size of the Cu–Ni–Sn–Ti–Cr and Cu–Ni–Sn–Ti–Cr–Ce alloys. In Fig. 6(a) the grains are oriented along the <110> direction in

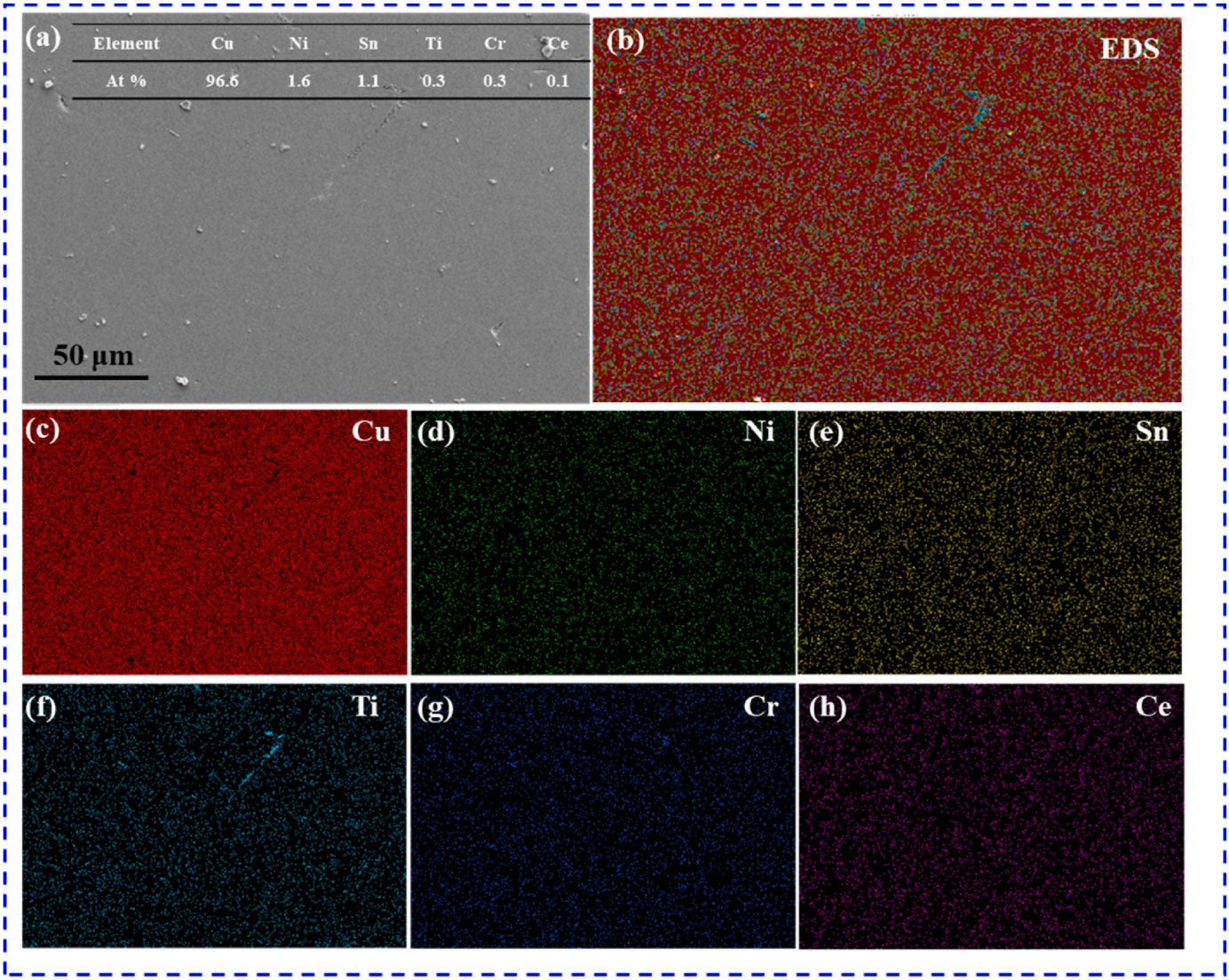

Fig. 4. Elements distribution in the Cu–Ni–Sn–Ti–Cr–Ce alloy after solution treatment: (a) SEM image, (b) combined EDS map, (c) Cu, (d) Ni, (e) Sn, (f) Ti, (g) Cr, and (h) Ce elemental maps.

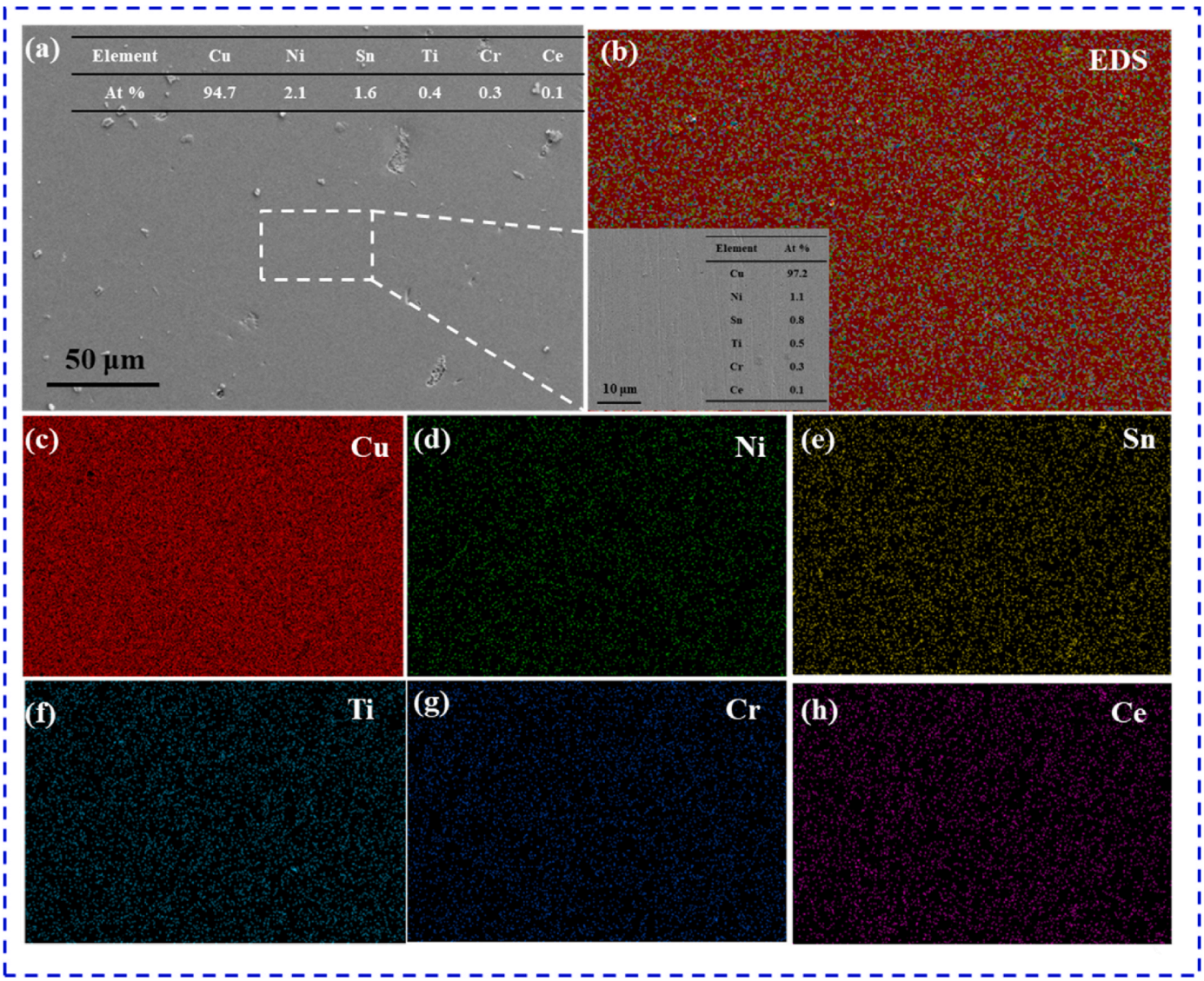

Fig. 5. Elements distribution in the Cu–Ni–Sn–Ti–Cr–Ce alloy after peak-aging: (a) SEM image, (b) combined EDS map, (c) Cu, (d) Ni, (e) Sn, (f) Ti, (g) Cr, and (h) Ce elemental maps.

the Cu–Ni–Sn–Ti–Cr alloy aged at 500 °C for 60 min. The average grain size is 286.4 μm and 61% of the grains are larger than 200 μm. Fig. 6(b) shows the EBSD diagram and grain size of the Cu–Ni–Sn–Ti–Cr alloy aged for 240 min. The grain orientation of the alloy is mainly along the <100> direction, the number of recrystallized grains increased, and the proportion of grains larger than 200 μm increased to 74%. The main reason is that the nuclei of fine crystalline grains in the alloy had enough time to form and grow and the grains of the alloy had enough time to grow. In addition, there are some twins in Fig. 6(b), which may be caused by the cold deformation of the alloy. Fig. 6(c) and (d) show the EBSD plots and grain size of the Cu–Ni–Sn–Ti–Cr–Ce alloy after 500 °C aging for 60 min and 240 min. The average grain size increased from 135 μm to 178 μm, and the proportion of grains larger than 200 μm increased from 31% to 51% with the aging time increased from 60 min to 240 min in Fig. 6(c) and (d). The smaller the grain size, the higher the strength and hardness of the alloy. Therefore, the hardness of Cu–Ni–Sn–Ti–Cr–Ce alloy aged at 500 °C for 60 min is higher than for 240 min, which is consistent with the data in Fig. 3(d). The average grain size of the Cu–Ni–Sn–Ti–Cr–Ce alloy and the proportion of grains larger than 200 μm are much smaller than the Cu–Ni–Sn–Ti–Cr alloy in Fig. 6(a) and (c), indicating that the micro-addition of Ce can refine the grains of the Cu–Ni–Sn–Ti–Cr alloy. Thus, the strength and hardness of the alloy are improved. The micro-hardness of the Cu–Ni–Sn–Ti–Cr–Ce alloy aged at 500 °C for 60 min is 245 HV, higher than the Cu–Ni–Sn–Ti–Cr alloy 221 HV, which confirms the idea that the micro-hardness of the Cu–Ni–Sn–Ti–Cr alloy can be improved by the micro-addition of Ce.

The dislocation existing in the alloy has an important impact on the strength, conductivity and other properties of the alloy. The dislocation density (ρ) can be calculated according to the data in KAM diagram [37]:

$$\rho = 2\theta/\mu b \tag{1}$$

Here, ρ is the dislocation density of the alloy (m^{-2}), θ is the mean orientation angle in the alloy KAM map (rad), μ is the scanning step length (μm), and b is Burger's vector of copper (0.255 nm).

According to Fig. 7(a) and (c), the dislocation density of the Cu–Ni–Sn–Ti–Cr alloy aged at 500 °C for 60 min and 240 min is $\rho = 9.25 \times 10^{15}$ m^{-2} and $\rho = 8.6 \times 10^{15}$ m^{-2}, respectively. According to Fig. 7(e) and (g), the dislocation density of the Cu–Ni–Sn–Ti–Cr–Ce alloy aged at 500 °C for 60 min and 240 min is $\rho = 7.34 \times 10^{15}$ m^{-2} and $\rho = 8.25 \times 10^{15}$ m^{-2}, respectively. By comparing Fig. 7(a) and (e), Fig. 7(c) and (g), it can be found that the dislocation density of the Cu–Ni–Sn–Ti–Cr–Ce

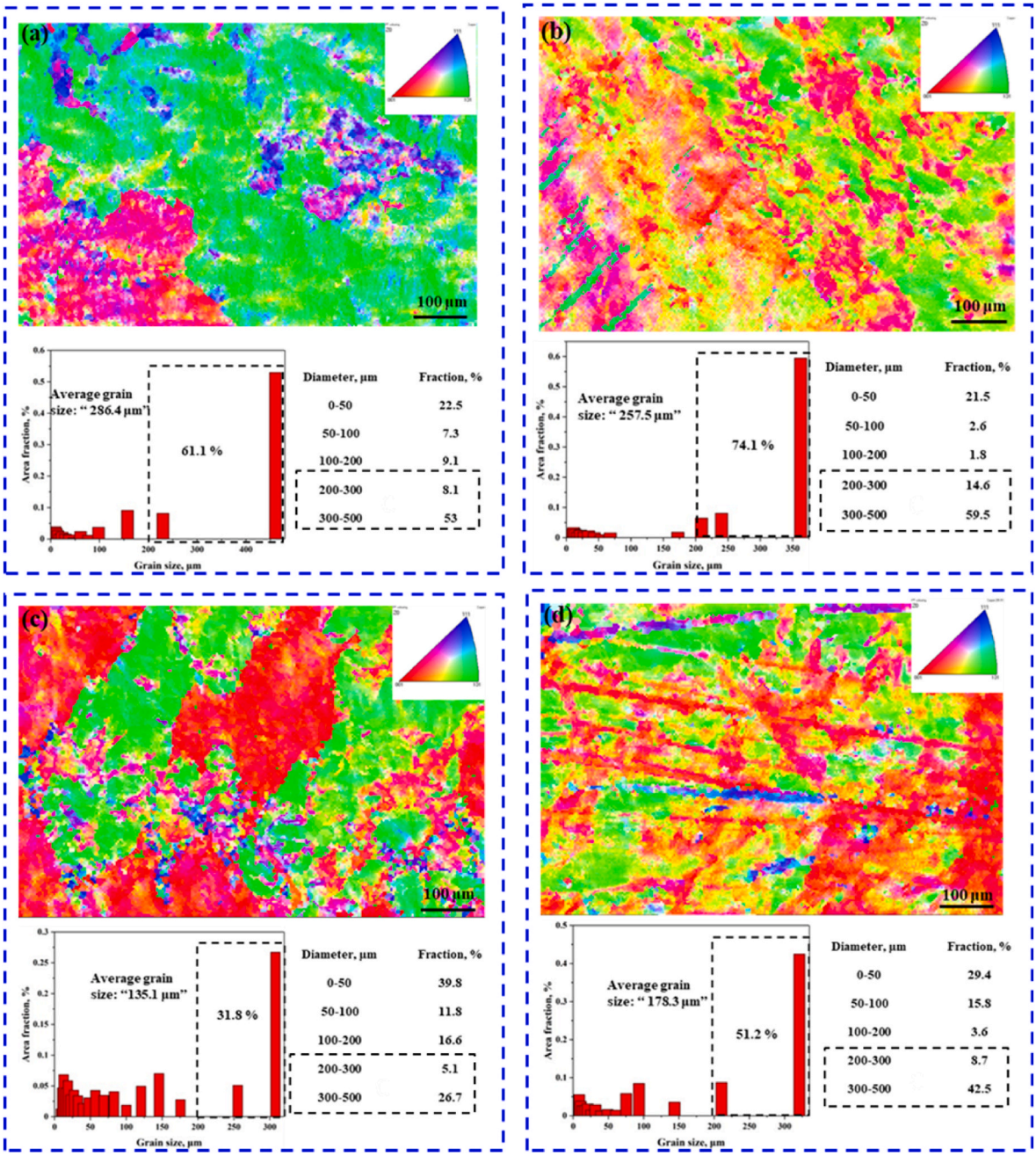

Fig. 6. EBSD maps and grain size of the Cu–Ni–Sn–Ti–Cr and Cu–Ni–Sn–Ti–Cr–Ce alloys: (a) Cu–Ni–Sn–Ti–Cr aged for 60 min, (b) Cu–Ni–Sn–Ti–Cr aged for 240 min, (c) Cu–Ni–Sn–Ti–Cr–Ce aged for 60 min, (d) Cu–Ni–Sn–Ti–Cr–Ce aged for 240 min.

alloy is lower than the Cu–Ni–Sn–Ti–Cr alloy, which indicates that the micro-addition of Ce can promote the dynamic recrystallization. The main reason is that dynamic recrystallization occurs by consuming dislocations to provide energy [38]. The dynamic recrystallization of the alloy produces fine grains, resulting in a fine-grain effect, and thus improves the strength and hardness of the alloy. Therefore, the hardness of the Cu–Ni–Sn–Ti–Cr–Ce alloy is greater than the Cu–Ni–Sn–Ti–Cr alloy. When the orientation angle of grains on both sides of the grain boundary is small, the grain boundary migration speed is small, which is not conducive to the formation of fine dynamically recrystallized grains [39, 40]. When the orientation angle is above 15°, the larger the orientation angle is, the more alloy can form fine dynamically recrystallized grains, to improve its strength and hardness. By comparing Fig. 7(b) and (f), it can be found that the large angle grain boundary values of the Cu–Ni–Sn–Ti–Cr–Ce alloy are larger than the Cu–Ni–Sn–Ti–Cr alloy, which indicates that the micro-addition of Ce can promote the formation of fine dynamically recrystallized grains, and improve the strength and hardness. As seen in Fig. 7(f) and (h), the large angle grain boundary value of the Cu–Ni–Sn–Ti–Cr–Ce alloy is 14.9% aged at 500 °C for 60 min. With the aging time increasing to 240 min, the large angle grain boundary value of the alloy decreases to 6.5%. Therefore, the strength and hardness of the Cu–Ni–Sn–Ti–Cr–Ce alloy aged for 60 min are greater than for 240 min, which is consistent with curves in Fig. 3(d) and (g). The Ce micro-addition can promote dynamic recrystallization, which increases the strength and hardness of the alloy. Dynamic recrystallization of the alloy mainly occurs during the aging phase shown in Fig. 1, as aging of the alloy at 500 °C provides sufficient energy for nucleation and growth of recrystallized grains.

In order to analyze the texture evolution of the Cu–Ni–Sn–Ti–Cr and Cu–Ni–Sn–Ti–Cr–Ce alloys under different aging conditions, the polar

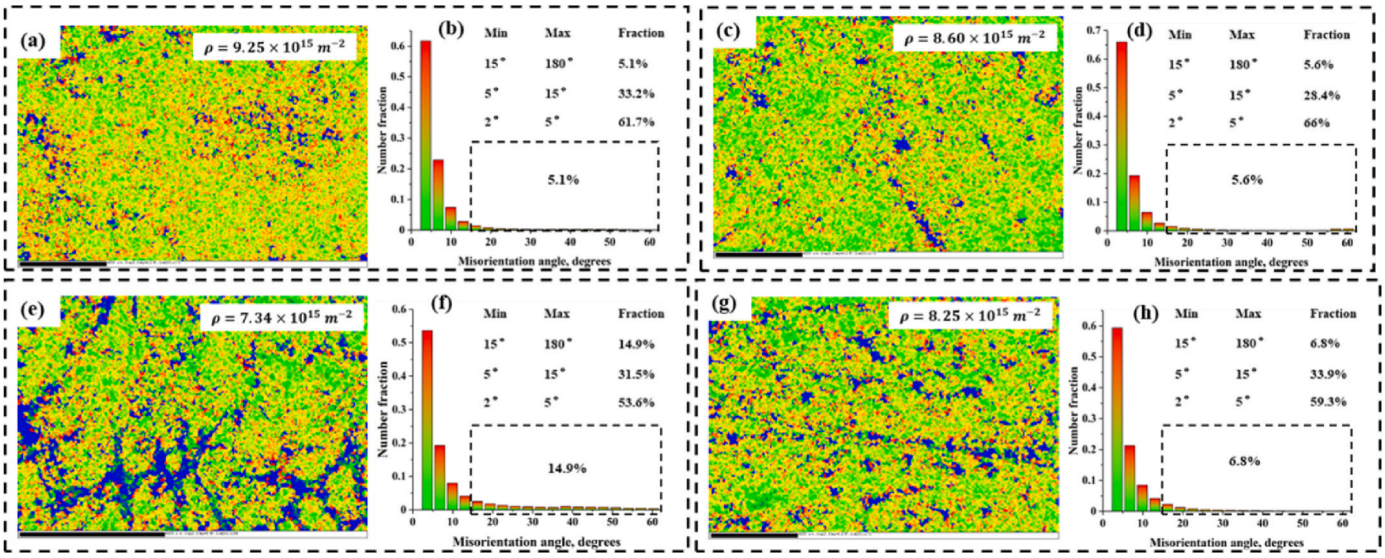

Fig. 7. Kernel average misorientation angle maps and misorientation angles distribution of Cu–Ni–Sn–Ti–Cr and Cu–Ni–Sn–Ti–Cr–Ce alloys: (a) and (b) Cu–Ni–Sn–Ti–Cr aged for 60 min, (c) and (b) Cu–Ni–Sn–Ti–Cr aged for 240 min, (e) and (f) Cu–Ni–Sn–Ti–Cr–Ce aged for 60 min, (g) and (h) Cu–Ni–Sn–Ti–Cr–Ce aged for 240 min.

diagram was obtained in Fig. 8, and the texture composition diagram in Fig. 9. Fig. 8 shows the polar plots and the (001), (011) and (111) directional texture types for both alloys. The main texture of the Cu–Ni–Sn–Ti–Cr alloy is {001}<111> cubic texture after aging at 500 °C for 60 min and 240 min, but the main texture of the Cu–Ni–Sn–Ti–Cr–Ce alloy is {011}<100> Goss and {001}<100> Cubic texture. The maximum texture strength of the Cu–Ni–Sn–Ti–Cr–Ce alloy is 18.309 when the aging time is 60 min, and the maximum texture strength is 17.059 when the aging time is extended to 240 min. The maximum texture strength of the Cu–Ni–Sn–Ti–Cr–Ce alloy has little change. The higher performance of the Cu–Ni–Sn–Ti–Cr–Ce alloy after 60 min aging than after 240 min aging may be attributed to the {011}<100> Goss texture change to {001}<100> cubic texture. Fig. 9 shows the texture composition of the Cu–Ni–Sn–Ti–Cr and Cu–Ni–Sn–Ti–Cr–Ce alloys after 500 °C, 60 min, and 240 min aging. The Cu–Ni–Sn–Ti–Cr–Ce alloy is taken as an example to analyze the texture evolution. The ideal texture composition of the alloy aged at 500 °C for 60 min is shown in Fig. 9(a), where cubic, Goss, Brass, copper, S, <111>//X, <110>//X, and <100>//X texture have the corresponding proportions of 0.0322%, 64.1%, 0.145%, 7.44%, 0.108%, 9.05%, 0.0322%, and 71.5%, respectively. As seen in Fig. 8(b), with the aging time extending from 60 min to 240 min, the volume fraction of the main texture of the Cu–Ni–Sn–Ti–Cr alloy cubic, Goss, Brass, copper, and S texture decreased and the texture strength decreased slightly. It can be observed in Fig. 9(b) and (c) that the volume fraction of Goss, Brass, copper and S texture increased, and the texture was slightly enhanced due to the minor addition of Ce for the two alloys aged at 500 °C for 240 min. This shows that the properties of the alloy are related to its main texture, including cubic, Goss, Brass, copper, and S texture. The stronger the five main textures, the better the performance of the alloy.

3.3. Microscopic TEM analysis

The deformation structures such as deformation bands, dislocation tangles, dislocation walls, twins, and precipitates from the copper matrix are closely related to the properties of copper alloys [41,42]. Fig. 10 shows the TEM microstructure of the Cu–Ni–Sn–Ti–Cr alloy aged at 500 °C for 60 min. It can be seen from the bright field images in Fig. 10 (a) and (b) that there are multiple microstructure features such as precipitated phase, dislocation entanglements, and dislocation walls in the Cu–Ni–Sn–Ti–Cr alloy. The precipitated phase can strengthen the copper matrix, hinder the dislocation movement and improve the strength and hardness of the alloy. In addition, the precipitated phase can reduce the lattice distortion of the copper matrix in the alloy, thereby reducing the scattering effect of electrons and increasing the electrical conductivity of the alloy [43]. Fig. 10(c) and (d) show the HRTEM micrographs and fast Fourier transform (FFT) diagram of the alloy, where the nano-scale precipitates were found to be $CuNi_2Ti$ by calibration. Three planar directions were obtained: $(103)_{CuNi2Ti}$, $(200)_{CuNi2Ti}$, and $(10\bar{3})_{CuNi2Ti}$. Fig. 10 (e) shows the inverse FFT (IFT) diagram of nano-scale $CuNi_2Ti$. The spacing of the $(103)_{CuNi2Ti}$ crystal planes is 0.209 nm, 0.184 nm for the $(200)_{CuNi2Ti}$ crystal planes, 0.207 nm for the $(10\bar{3})_{CuNi2Ti}$ crystal planes, and no dislocations were found in the IFT map. By calibrating the FFT diagram of Fig. 10(f), it was determined that it was a copper matrix. The strip axis of the copper matrix was calculated to be $[0\bar{1}1]_{Cu}$, and the spacing of the $(200)_{Cu}$ crystal planes was measured to be 0.18 nm. The mismatch between the nanometer $CuNi_2Ti$ phase and Cu matrix is $\delta = \frac{2(d_\alpha - d_\beta)}{d_\alpha + d_\beta} = \frac{2\times(0.184-0.180)}{(0.184+0.180)} \times 100\% = 2.2\% < 5\%$, its interface is a coherent interface, where d_α and d_β are the crystal plane spacing of two parallel planes $(200)_{CuNi2Ti}$ and $(200)_{Cu}$, respectively. The precipitated phase and the matrix at the coherent interface have a low mismatch strain, which means that the coherent interface between the $CuNi_2Ti$ phase and the Cu matrix can improve the strength and hardness of the alloy without sacrificing plasticity [26]. In addition, precipitates with large sizes were also found in the Cu–Ni–Sn–Ti–Cr alloy, as seen in Fig. 11(a). According to the HRTEM of Fig. 11(b) and (d) and FFT of Fig. 11(e), the larger precipitated phase is Cr. Fig. 11(c) shows the XRD image of the larger precipitated phase in Fig. 11(a). The proportion of Cr atoms in the precipitated phase is 94.6%, which verifies that the precipitated phase is Cr. The crystal plane spacing of $(011)_{Cr}$ is 0.207 nm as seen in Fig. 11(e), (f), and (g), while the crystal plane spacing of $(211)_{Cu}$ in the parallel plane of the copper matrix is 0.181 nm in Fig. 11(h), (i) and (j). The mismatch between the Cr phase and Cu matrix is $5\% < \delta = \frac{2\times(0.207-0.181)}{(0.207+0.181)} \times 100\% = 13.4\% < 15\%$, and its interface is semi-coherent. The precipitated phase of the semi-coherent interface with a low mismatch degree produces small elastic stress and low interfacial energy, which plays an important role in improving the strength and hardness of the alloy [44]. Fig. 11(k) is the GPA diagram of Fig. 11(d). According to the color change and scale of the GPA diagram, the color of the Cr phase is light white represented by the +0.1 scale, which represents compressive stress and

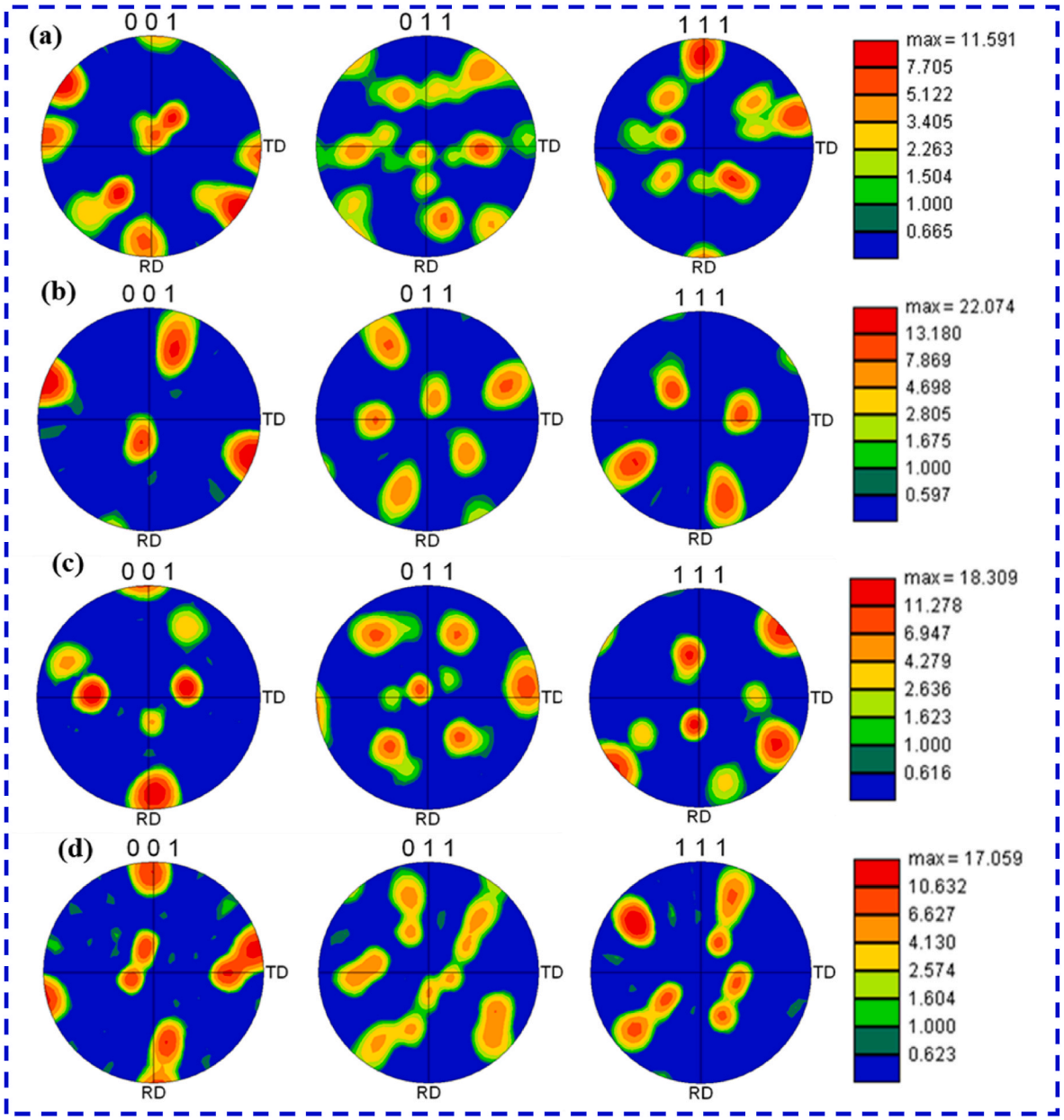

Fig. 8. Pole figures of the Cu–Ni–Sn–Ti–Cr and Cu–Ni–Sn–Ti–Cr–Ce alloys: (a) Cu–Ni–Sn–Ti–Cr aged for 60 min, (b) Cu–Ni–Sn–Ti–Cr aged for 240 min, (c) Cu–Ni–Sn–Ti–Cr–Ce aged for 60 min, (d) Cu–Ni–Sn–Ti–Cr–Ce aged for 60 min.

most of it is uniform strain, while the color of Cu is dark blue represented by the −0.1 scale, which represents tensile stress and most of it is uniform strain. The interaction between compressive and tensile stresses and lattice distortion of the Cr phase and Cu matrix play an important role in strengthening the Cu–Ni–Sn–Ti–Cr alloy and improving its hardness.

Fig. 12 shows TEM and HRTEM images of the Cu–Ni–Sn–Ti–Cr–Ce alloy aged at 500 °C for 60 min. It can be seen from the bright field images in Fig. 12(a), (b), and (c) that there is a typical microstructure containing deformation bands, dislocation tangles, and dislocation lines in the Cu–Ni–Sn–Ti–Cr–Ce alloy. In addition, there is a large number of nano-scale precipitates. Fig. 12(d) shows the dark-field image of (c), which can more intuitively reflect the distribution of nano-scale precipitates in the Cu–Ni–Sn–Ti–Cr–Ce alloy. Fig. 12(e) is the HRTEM image of nano-scale precipitated $CuNi_2Ti$, and Fig. 12(f) is its FFT diagram. Three planar orientations of $(112)_{CuNi2Ti}$, $(200)_{CuNi2Ti}$ and $(1\overline{1}2)_{CuNi2Ti}$ were obtained. The zone axis of the nano-sized precipitated $CuNi_2Ti$ was calculated as $[02\overline{1}]_{CuNi2Ti}$. Fig. 12(g) shows the grayscale spectrum in the vertical direction of the $(112)_{CuNi2Ti}$ crystal plane, which is the measurement of the crystal plane spacing of the $(112)_{CuNi2Ti}$ crystal plane. It was obtained that $d_{(1\ 1\ 2)} = 0.217$ nm. Fig. 12(h) shows the small area diffraction pattern (SADP) image of the copper matrix and the grayscale spectrum of the $(111)_{Cu}$ crystal plane in the vertical direction, and the spacing of the $(111)_{Cu}$ crystal plane is 0.213 nm. The mismatch between the nano-precipitated $CuNi_2Ti$ phase and the Cu matrix is calculated from two parallel planes $(112)_{CuNi2Ti}$ crystal plane and $(111)_{Cu}$ crystal plane: $\delta = \frac{2\times(0.217-0.213)}{(0.217+0.213)} \times 100\% = 1.9\% < 5\%$. This indicates that the interface between the nano-precipitated $CuNi_2Ti$ phase and Cu matrix in the Cu–Ni–Sn–Ti–Cr–Ce alloy is the same as the Cu–Ni–Sn–Ti–Cr alloy, which is beneficial to improve the strength and hardness. In addition, a precipitated phase with a large size was also found in the Cu–Ni–Sn–Ti–Cr–Ce alloy, as seen in Fig. 12(i). Fig. 12(j) and (k) show the HRTEM and FFT plots of the precipitated phase, respectively. The precipitated phase was found to be the NiTi phase by

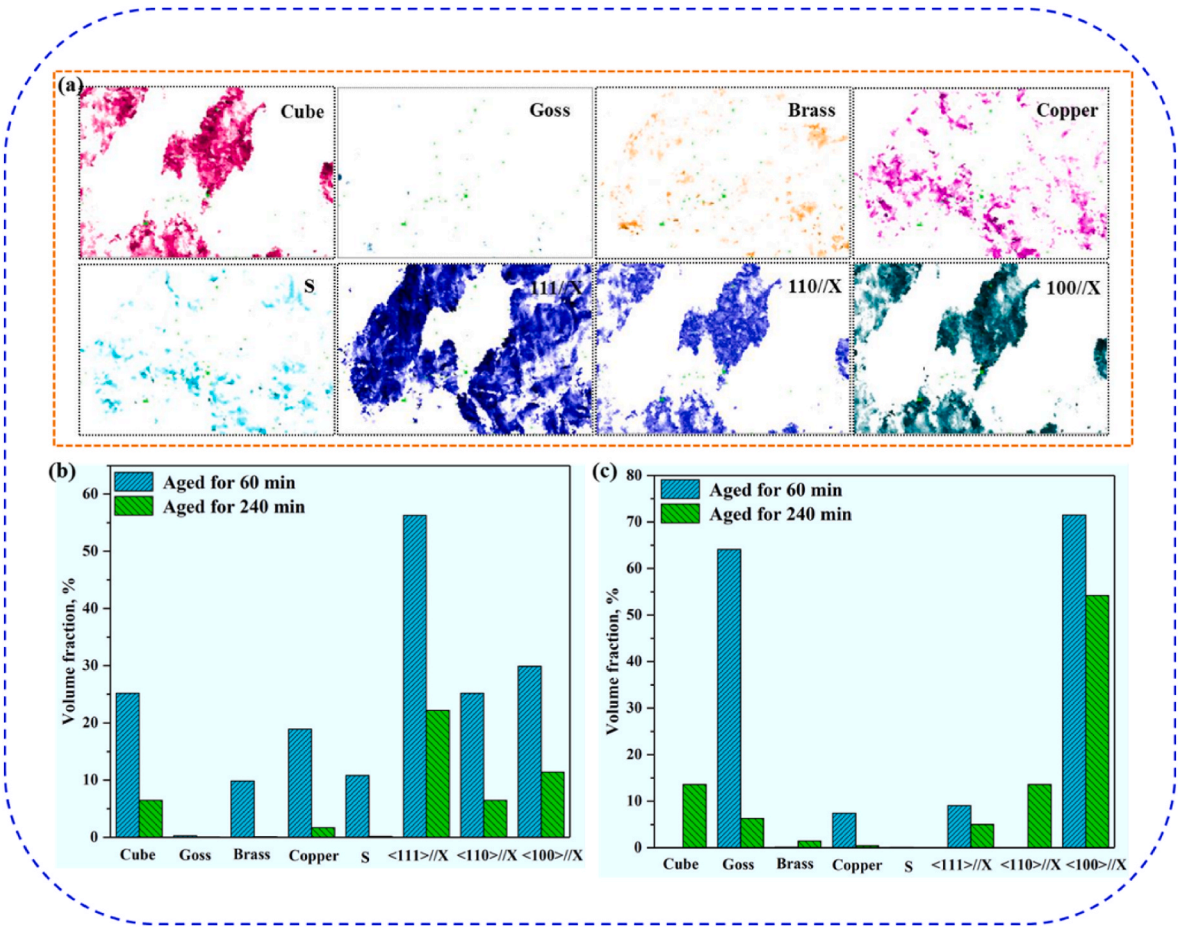

Fig. 9. Texture composition of the Cu–Ni–Sn–Ti–Cr and Cu–Ni–Sn–Ti–Cr–Ce alloys: (a) Cu–Ni–Sn–Ti–Cr–Ce aged for 60 min, (b) Cu–Ni–Sn–Ti–Cr and (c) Cu–Ni–Sn–Ti–Cr–Ce alloys aged at 500 °C for 60 and 240 min.

calibration. Fig. 13 shows the EDS and element distribution of the Cu–Ni–Sn–Ti–Cr–Ce alloy aged at 500 °C for 60 min obtained in TEM. It is known that Ni and Cu are infinitely miscible, and combined with the distribution of elements in Fig. 13, some Ni atoms of the Cu–Ni–Sn–Ti–Cr–Ce alloy replace Cu atoms to form $CuNi_2Ti$ and NiTi phases. It can be seen from Fig. 13(g) that there are still many Cr atoms in the Cu–Ni–Sn–Ti–Cr–Ce alloy, so there are nano-scale Cr phases in the Cu–Ni–Sn–Ti–Cr–Ce alloy. In the aging experiment of copper alloy, the solute atoms in the solid solution in the copper matrix are precipitated. The precipitated phase enhances the copper matrix, improves the strength and hardness of the alloy, and reduces the lattice distortion of the copper matrix, thus reducing the scattering effect of electrons and improving the conductivity of the alloy, so that the alloy has good properties [45].

4. Discussion

4.1. Ce micro-addition effects on properties

The above results indicate that the designed Cu–Ni–Sn–Ti–Cr and Cu–Ni–Sn–Ti–Cr–Ce alloys have good mechanical properties and electrical conductivity after homogeneous annealing, solution, cold rolling, and aging treatments. The precipitated phase of $CuNi_2Ti$ and NiTi in the alloy or the intermetallic compound particles in the alloy can effectively hinder the dislocations formed in the cold deformation process, and effectively enhance the strength and hardness [46]. The micro-hardness of the Cu–Ni–Sn–Ti–Cr alloy aged at 500 °C for 0–480 min is plotted in Fig. 3(a), and the micro-hardness of the Cu–Ni–Sn–Ti–Cr alloy from short to long aging time is 138 HV, 178 HV, 189 HV, 204 HV, 221 HV, 199 HV, 176 HV, 162 HV, and 152 HV. The micro-hardness of the Cu–Ni–Sn–Ti–Cr–Ce alloy aged at 500 °C for 0–480 min is plotted in Fig. 3(d), and the micro-hardness from short to long aging time is 146 HV, 168 HV, 189 HV, 216 HV, 245 HV, 220 HV, 196 HV, 193 HV, and 169 HV. The micro-hardness can be improved by the micro-addition of Ce comparing the Cu–Ni–Sn–Ti–Cr and Cu–Ni–Sn–Ti–Cr–Ce alloys aged at 500 °C for 0–480 min. According to Fig. 3(c) and (f), the peak micro-hardness of the Cu–Ni–Sn–Ti–Cr–Ce alloy aged at 400–550 °C is significantly higher than the Cu–Ni–Sn–Ti–Cr alloy, and the peak electrical conductivity of the Cu–Ni–Sn–Ti–Cr–Ce alloy aged at 400–550 °C is slightly lower than the Cu–Ni–Sn–Ti–Cr alloy. This indicates that the micro-addition of Ce significantly improves the hardness of the alloy with slightly reduced electrical conductivity. According to Fig. 3(g) and (h), the tensile strength of the Cu–Ni–Sn–Ti–Cr–Ce alloy is greater than the Cu–Ni–Sn–Ti–Cr alloy at the same aging temperature and time, and the elongation is slightly lower than the Cu–Ni–Sn–Ti–Cr alloy. After aging at 500 °C for 60 min, the tensile strength of the Cu–Ni–Sn–Ti–Cr alloy was 598.1 MPa and the elongation was 9.9%, while the tensile strength of the Cu–Ni–Sn–Ti–Cr–Ce was 645.2 MPa and the elongation was 9.4%. Compared with Fig. 6(b) and (d), the average grain size of the Cu–Ni–Sn–Ti–Cr alloy and the proportion of grain size larger than 200 μm is 257.5 μm and 74%, respectively. Both of them are much larger than the 178.3 μm and 51% of the Cu–Ni–Sn–Ti–Cr–Ce, indicating that the micro-addition of Ce can refine the grain and improve the strength and hardness of the alloy. Under the same aging conditions, compared with the Cu–Ni–Sn–Ti–Cr–Ce alloy, the Cu–Ni–Sn–Ti–Cr–Ce alloy has higher hardness and tensile strength. However, the conductivity and elongation of the Cu–Ni–Sn–Ti–Cr alloy are slightly higher than the Cu–Ni–Sn–Ti–Cr–Ce alloy. In general, the Cu–Ni–Sn–Ti–Cr–Ce alloy has

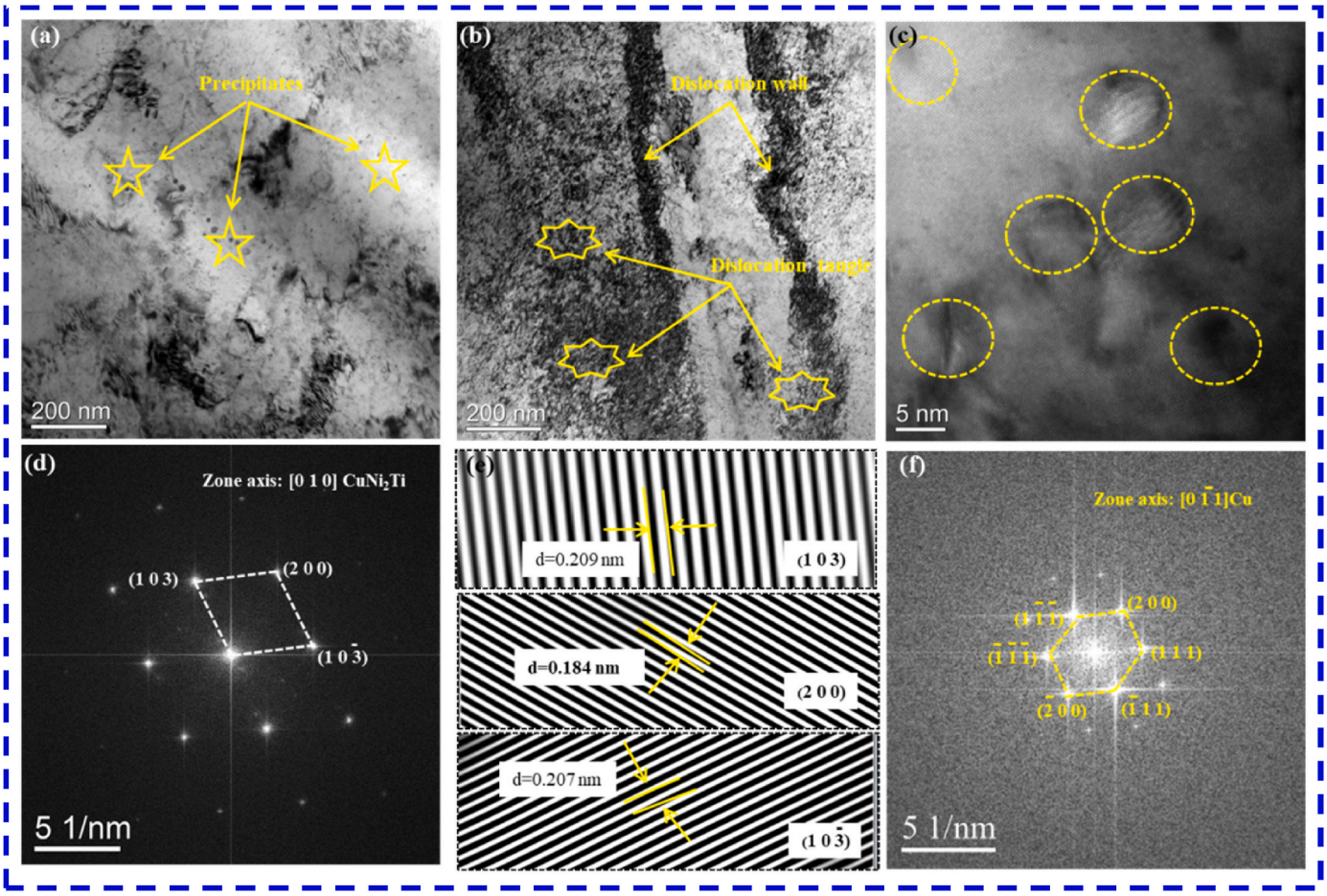

Fig. 10. TEM microstructure of Cu–Ni–Sn–Ti–Cr alloy aged at 500 °C for 60 min: (a) and (b) bright-field images, (c) HRTEM micrograph of $CuNi_2Ti$, (d) FFT pattern of $CuNi_2Ti$, (e) IFT pattern of $CuNi_2Ti$, (f) FFT pattern of Cu.

better comprehensive properties than the Cu–Ni–Sn–Ti–Cr alloy.

4.2. Ce micro-addition effects on texture and precipitates

The texture evolution of the alloy during aging can be determined by the polar diagrams and the texture component diagrams. The type, texture strength, and proportion of the texture in the alloy are closely related to the properties of the alloy [36]. It can be seen from Fig. 8 that the main texture of the Cu–Ni–Sn–Ti–Cr alloy aged at 500 °C for 60 min is {001}<111>, and the maximum texture strength is 11.591. The main texture of the Cu–Ni–Sn–Ti–Cr–Ce alloy aged at 500 °C for 60 min is {011}<100> Goss texture, and the maximum texture strength is 18.309. These results indicate that the micro-addition of Ce can change the texture type and increase the maximum texture strength of the alloy. As seen in Fig. 8, the texture groups of the Cu–Ni–Sn–Ti–Cr alloy aged at 500 °C for 240 min were cubic, Goss, Brass, copper texture, S, <111>//X, <110>//X, and <100>//X texture with the corresponding proportions of 6.47%, 0.0645%, 0.12%, 1.69%, 0.193%, 22.2%, 6.47%, and 11.4%. For the Cu–Ni–Sn–Ti–Cr–Ce alloy, the corresponding texture proportions are 13.6%, 6.32%, 1.47%, 0.481%, 0.0115%, 5.04%, 13.6%, and 54.2%. After Ce micro-addition, the volume fraction of Brass texture and copper texture decreased slightly, while the volume fraction of cubic texture, Goss texture, and S texture increased significantly, indicating that the Ce micro-addition can change the volume fraction and texture strength of the alloy. The higher properties of the Cu–Ni–Sn–Ti–Cr–Ce alloy aged at 500 °C for 240 min may be attributed to the higher volume fraction of cubic, Goss, and S texture in the alloy. In addition to the alloy texture effects on its properties, the precipitation in the alloy is relatively important to enhance its strength and hardness. As seen in Figs. 10 and 11, the nano-scale precipitated phase in the Cu–Ni–Sn–Ti–Cr alloy is the $CuNi_2Ti$ phase, and the precipitated phase with a large size is the Cr phase. The nanoscale precipitated phase in the Cu–Ni–Sn–Ti–Cr–Ce alloy is the $CuNi_2Ti$ phase, and the precipitated phase with a larger size is the NiTi phase, as seen in Fig. 12. By comparing Figs. 10(a) and Fig. 12(d), it can be seen that the number of nano-scale precipitates in the Cu–Ni–Sn–Ti–Cr–Ce alloy is significantly higher than in the Cu–Ni–Sn–Ti–Cr alloy, and the precipitates are smaller. This indicates that the Ce micro-addition is conducive to the precipitation of the NiTi phase, which can promote the refinement and precipitation of the nano-scale precipitated phase in the alloy, and enhance the strength and hardness of the alloy. In addition, the nanocrystalline precipitates from the copper alloy matrix decrease the electron scattering effects and increase the alloy's electrical conductivity.

4.3. Strengthening and conductivity mechanisms

The strengthening mechanisms of copper alloys can be divided into four types (solution, deformation, grain boundary, and precipitation strengthening), among which precipitation strengthening is the main strengthening mechanism of aged copper alloys. The yield strength σ of the Cu–Ni–Sn–Ti–Cr–Ce alloy is mainly composed of the following five parts [47]:

$$\sigma = \sigma_0 + \sigma_{ss} + \sigma_{ds} + \sigma_p + \sigma_{GB} \quad (2)$$

Here, σ_0 is the lattice friction stress of the Cu matrix, 20 MPa [48]. σ_{ss} is the stress of solution strengthening, σ_{ds} is the stress of work hardening,

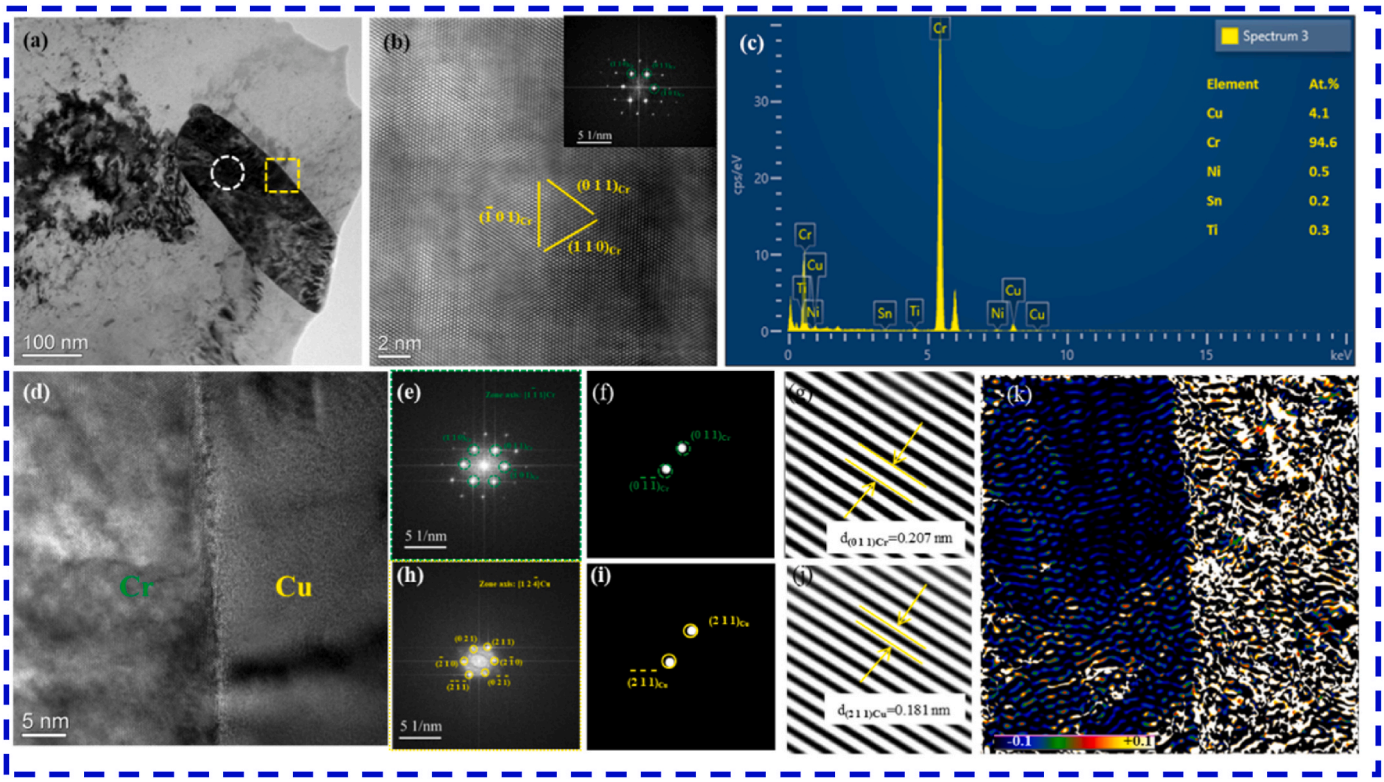

Fig. 11. HRTEM images and microstructure of the Cu–Ni–Sn–Ti–Cr alloy aged at 500 °C for 60 min: (a) bright field image, (b) HRTEM images of the white circle area in (a), (c) EDS spectra of Cr in (b), (d) HRTEM images of the yellow rectangular region in (a), (e) FFT pattern of Cr, (f) and (g) IFT pattern of Cr, (h) FFT pattern of Cu, (i) and (j) IFT pattern of Cu, (k) GPA map of (d). (For interpretation of the references to color in this figure legend, the reader is referred to the Web version of this article.)

σ_p is the stress of precipitation strengthening, and σ_{GB} is the stress of grain boundary strengthening. Solid solution strengthening is related to the radius difference between solute Ni, Sn, Ti, Cr, and Ce atoms and copper matrix atoms. The degree of solid solution strengthening can be described as follows [27]:

$$\sigma_{ss} = G\left(|\delta| + \frac{1}{20}\right)|\eta|^{\frac{3}{2}}\sqrt{\frac{x_a}{3}} \tag{3}$$

Here, G is the shear modulus of copper alloy (G = 46 GPa), δ is the lattice change factor caused by solution alloying (δ = 0.1105), η is the factor describing the shear modulus change caused by solution alloying (η = 0.3171), and x_a is the fraction of solute atoms in the solid solution. The contents of Ni, Sn, Ti, Cr, and Ce in the alloy are 1.1%, 0.8%, 0.5%, 0.3%, and 0.1%, as shown in Fig. 5(b) x_a = 1.1% +0.8%+0.5% + 0.3%+ 0.1% = 2.8%. Therefore, the solution strengthening degree σ_{ss} of the Cu–Ni–Sn–Ti–Cr–Ce alloy can be calculated as 127.3 MPa.

The effect of grain boundary strengthening can be expressed by the Hall-Petch formula [49]:

$$\sigma_{GB} = K_y d^{-1/2} \tag{4}$$

Here, K_y is the Hall-Petch coefficient, which is equal to 150 MPa $\mu m^{1/2}$, d is the average grain size, which is 135 μm. Therefore, the grain boundary strengthening σ_{GB} of the Cu–Ni–Sn–Ti–Cr–Ce alloy can be calculated as 12.9 MPa.

In order to improve the strength and hardness of the Cu–Ni–Sn–Ti–Cr–Ce alloy, the alloy after the solution strengthening was cold-rolled with 60% deformation. The deformation bands, dislocations, deformation twins, and other structures generated by cold rolling strengthened the copper matrix. The effect of deformation strengthening can be described as follows [50]:

$$\sigma_{ds} = M\alpha Gb\sqrt{\rho} \tag{5}$$

Here, M is the Taylor coefficient (3.06), α is the geometric constant (0.3), G is the shear modulus (46 GPa), b is the Burgers vector (0.2556 nm), ρ is the dislocation density of the alloy. Therefore, the deformation strengthening σ_{ds} of the Cu–Ni–Sn–Ti–Cr–Ce alloy can be calculated as 185 MPa.

The type and size of the precipitated phase in the Cu–Ni–Sn–Ti–Cr–Ce alloy and the relationship between the precipitated phase and dislocations play an important role in the strengthening of the alloy. The relationship between the precipitated phase and dislocations in the copper alloy is usually a bypass mechanism. The effect of precipitation strengthening caused by the bypass mechanism (Orowan-Ashby equation) of the Cu–Ni–Sn–Ti–Cr–Ce alloy can be described as follows [51]:

$$\sigma_p = 0.81 \times \frac{Gb}{2\pi(1-\upsilon)^{1/2}} \times \frac{\ln\left(d_p/b\right)}{(\lambda - d_p)} \tag{6}$$

Here, G is the shear modulus of copper (G = 46 GPa), b is the Burgers vector (b = 0.2556 nm), ν is Poisson's ratio (0.34), d_p is the average precipitated particle size (d_p = 24.6 nm), and λ is the spacing between particles on the slip plane, which is related to the average precipitated particle size d_p. Thus, λ can be expressed as follows:

$$\lambda = \frac{1}{2}d_p\sqrt{\frac{3\pi}{2f_p}} \tag{7}$$

Here, f_p is the volume fraction of the secondary phase particles (f_p = 4.1%). Therefore, the precipitation strengthening degree σ_p of the Cu–Ni–Sn–Ti–Cr–Ce alloy can be calculated as 312.1 MPa. In the end, the yield strength σ of the Cu–Ni–Sn–Ti–Cr–Ce alloy is $\sigma = \sigma_0 + \sigma_{ss} + \sigma_{ds} + \sigma_p + \sigma_{GB}$ = 20 + 127.3+185 + 312.1+12.9 = 657.3 MPa. This is slightly higher than the measured value (645.2 MPa), which is mainly

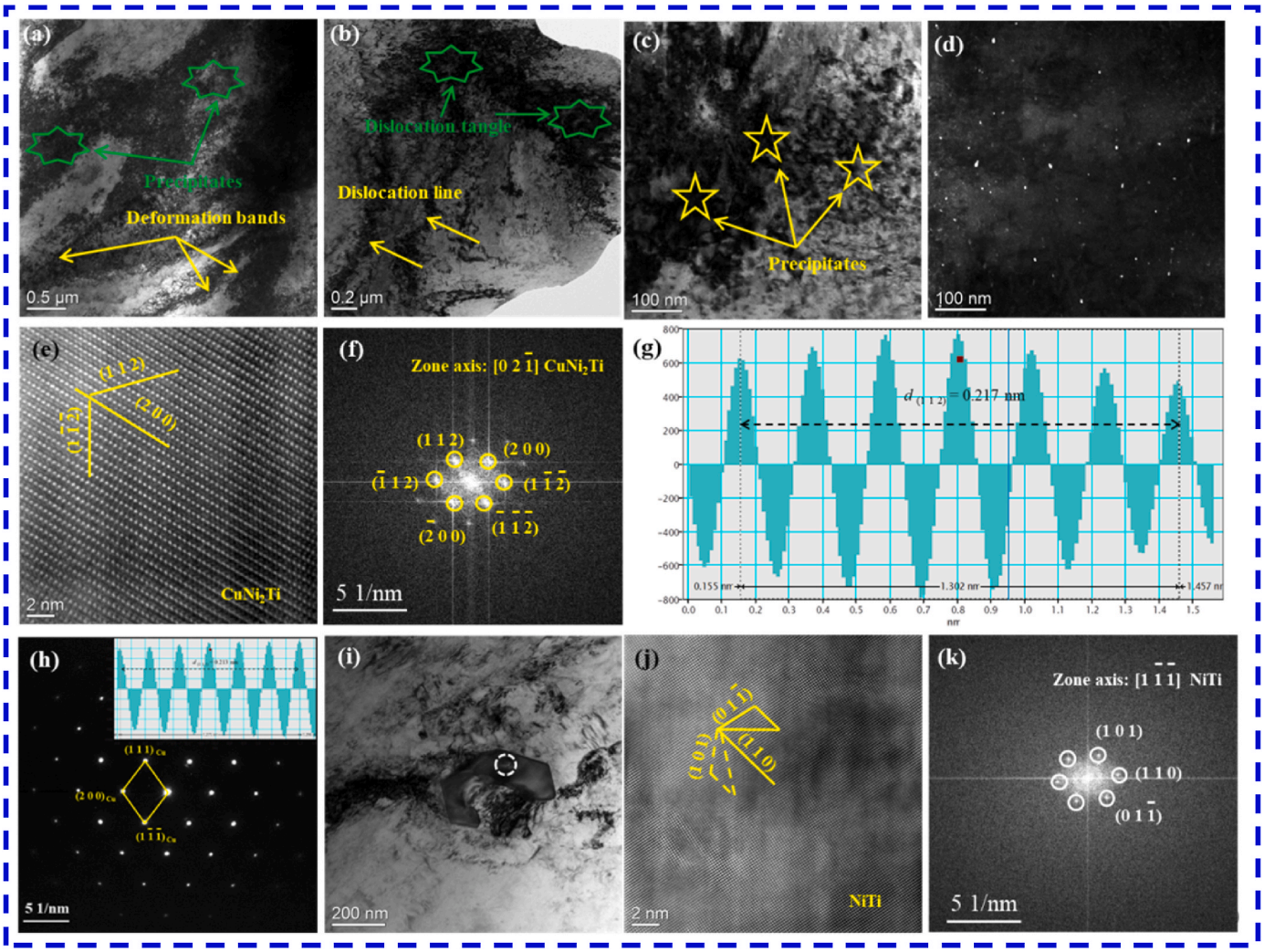

Fig. 12. TEM and HRTEM images of the Cu–Ni–Sn–Ti–Cr–Ce alloy aged at 500 °C for 60 min: (a–c), (i) bright field images, (d) dark field image showing the precipitates' distribution, (e) HRTEM micrograph of $CuNi_2Ti$, (f) FFT pattern of $CuNi_2Ti$, (g) gray-scale spectrogram of the vertical direction of crystal plane in (e), (h) diffraction spots of the matrix, (j) HRTEM micrograph of NiTi, (k) FFT pattern of NiTi.

related to the larger size of the particles equal to the Cr and NiTi phases.

In addition, for the conductivity of Cu–Ni–Sn–Ti–Cr–Ce alloy, the resistivity of copper alloy is related to dislocation, grain boundary and precipitated phase in the alloy. According to Matthiessen's rule [52], the resistivity can be expressed as:

$$\Omega = \Omega_{Cu} + \Omega_{Dis} + \Omega_{GB} + \Omega_P \tag{8}$$

Here, Ω_{Cu} is the resistivity of pure Cu ($\Omega_{Cu} = 1.724 \times 10^{-8}\ \Omega \bullet m$). Ω_{Dis} is the resistivity due to dislocation of the alloy, which can be expressed as:

$$\Omega_{Dis} = \rho \bullet \Omega_{PC} \tag{9}$$

Ω_{PC} is the resistivity of the dislocation caused by Cu ($\Omega_{PC} = 2 \times 10^{-25}\ \Omega \bullet m^3$) [53]. ρ is the dislocation density of the alloy, so the increased resistivity Ω_{Dis} for the dislocation density of Cu–Ni–Sn–Ti–Cr–Ce alloy can be calculated as $0.015 \times 10^{-8}\ \Omega \bullet m$. Moreover, the resistivity Ω_{GB} caused by alloy grain boundaries can be expressed as:

$$\Omega_{GB} = \frac{2}{3}\Omega_{Me-GB}\left(\frac{s}{v}\right) \tag{10}$$

Ω_{Me-GB} is the grain boundary resistivity caused by Cu ($\Omega_{Me-GB} = 2.04 \times 10^{-16}\ \Omega \bullet m^3$) [54], $\frac{s}{v}$ is the grain boundary area per volume, assuming that the grain of copper alloy is a tetrahedron, then $\frac{s}{v}$ is 2.37/d, The grain boundary resistivity of Cu–Ni–Sn–Ti–Cr–Ce alloy is $0.25 \times 10^{-8}\ \Omega \bullet m$. The resistivity Ω_P caused by precipitated phase can be expressed as:

$$\Omega_P = \Omega - \Omega_{Cu} - \Omega_{Dis} - \Omega_{GB} \tag{11}$$

The resistivity measured by Cu–Ni–Sn–Ti–Cr–Ce alloy($\Omega = 3.86 \times 10^{-8}\ \Omega \bullet m$), the resistivity caused by the precipitated phase of Cu–Ni–Sn–Ti–Cr–Ce alloy is $\Omega_P = \Omega - \Omega_{Cu} - \Omega_{Dis} - \Omega_{GB} = (3.86 - 1.72 - 0.015 - 0.25) \times 10^{-8} = 1.875 \times 10^{-8}\ \Omega \bullet m$. $\Omega_P > \Omega_{Cu} > \Omega_{GB} > \Omega_{Dis}$, from the alloy resistivity calculation results, Cu–Ni–Sn–Ti–Cr–Ce alloy caused by the precipitate phase is the largest resistivity, is the main factor affecting the alloy resistivity.

The calculation results of strengthening mechanism and resistivity of the alloy show that precipitation strengthening is the main factor affecting the strength of Cu–Ni–Sn–Ti–Cr–Ce alloy, and the precipitated phase is the main factor affecting the conductivity of the alloy. Several techniques have been used to control the interactions between the nano-precipitates and the matrix to improve the strength of the alloy, but the chaotic phase relationship between the nano-precipitate and the matrix often reduces the elongation of the alloy [55]. Generally speaking, the strength of the alloy is negatively correlated with elongation, and increasing the strength will reduce the elongation. The precipitated $CuNi_2Ti$ phase and the Cu matrix have coherent interfaces, and the

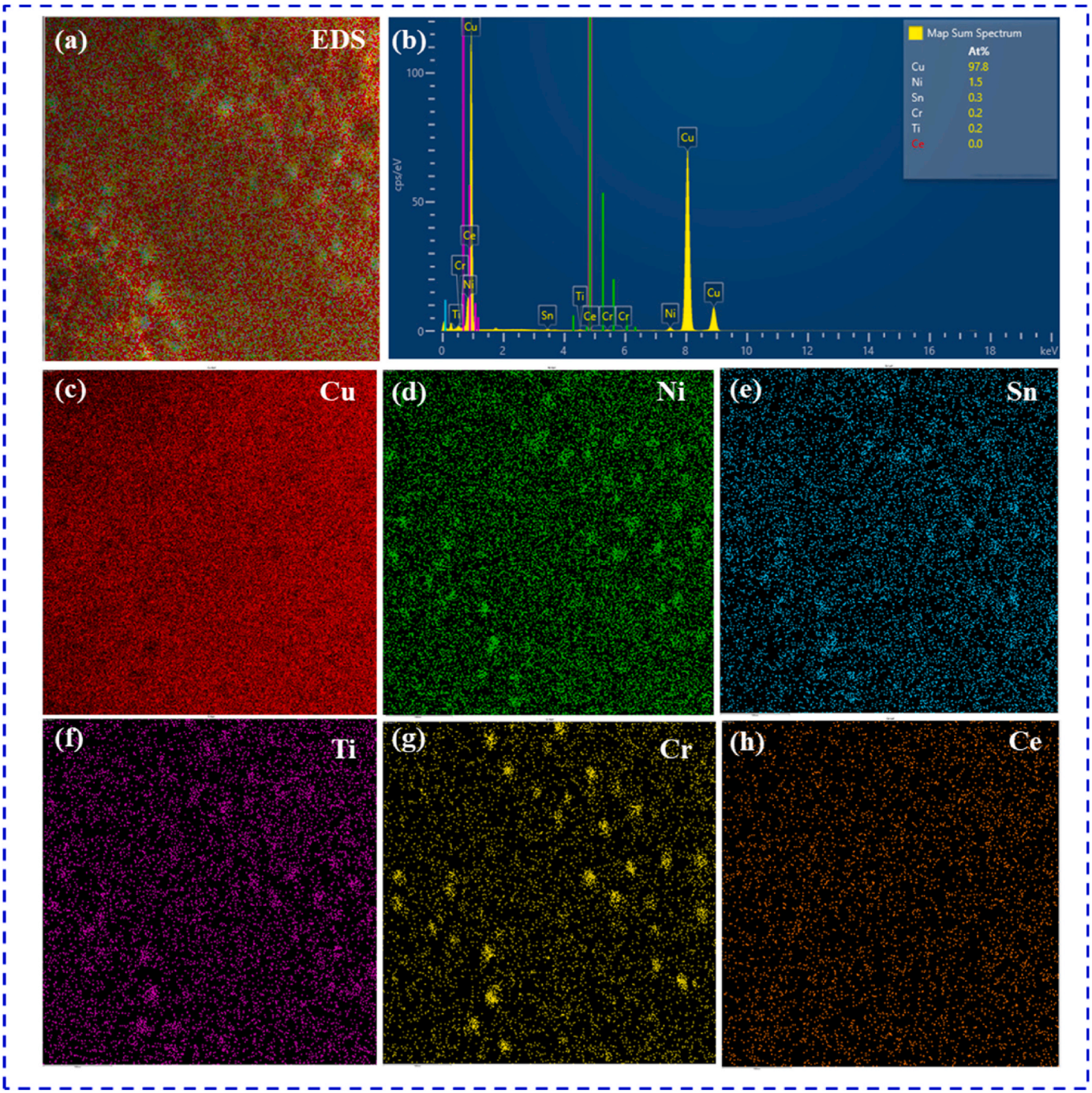

Fig. 13. EDS and element distribution of Cu–Ni–Sn–Ti–Cr–Ce alloy aged at 500 °C for 60 min under TEM: (a) EDS map, (b) EDS spectra, (c) Cu, (d) Ni, (e) Sn, (f) Ti, (g) Cr, and (h) Ce elemental maps.

precipitated phase and the matrix at the coherent interface have a low mismatch strain, which reduces the alloy cracking during deformation. This means that the nanoscale $CuNi_2Ti$ phase can improve the alloy strength and ductility. Precipitates constantly form in the alloy at the under-aged stage with increased aging time or temperature, improving its hardness and electrical conductivity in Fig. 3. At the peak-aging stage, the hardness of the alloy first increased to the maximum and then decreased, while the electrical conductivity continued to increase. The interaction is mainly between the precipitate's growth and the dynamic softening of the alloy. When the hardness of the alloy reaches the maximum, the dynamic softening dominates and the hardness of the alloy begins to decline. In the over-aging stage, dynamic softening plays a dominant role, and the hardness of the alloy decreases with the aging time.

5. Conclusions

The new Cu–Ni–Sn–Ti–Cr alloy has been designed with solution treatment, 60% cold rolling, and aging at 500 °C for 60 min, having 221 HV micro-hardness, 598.1 MPa tensile strength, 9.9% elongation, and 45.2% IACS conductivity. The new Cu–Ni–Sn–Ti–Cr–Ce alloy was also obtained by aging at 500 °C for 60 min, having 245 HV micro-hardness, 645.2 MPa tensile strength, 9.4% elongation and 44.6% IACS conductivity. It is observed that the micro-addition of rare earth Ce can refine

the grain of the Cu–Ni–Sn–Ti–Cr alloy, promote the formation of fine dynamically recrystallized grains, and significantly improve the microhardness and strength of the alloy. The excellent comprehensive properties of the alloy are attributed to the composite effects of solution strengthening, deformation, grain boundary, and precipitation strengthening, among which precipitation strengthening is the most important. The strengthening effect of precipitation is largely due to the presence of nano-scale $CuNi_2Ti$, Cr, and NiTi phases in the alloy. In addition, the nano-scale $CuNi_2Ti$ phase and Cu matrix interface is coherent, which can improve the strength and ductility of the alloy. The electrical conductivity increases with aging time mainly because the dynamic softening effects of the alloy and the precipitated phase reduce the distortion in the copper matrix and the scattering effect of electrons, leading to the continuous improvement of the electrical conductivity of the alloy.

CRediT authorship contribution statement

Shunlong Tang: Investigation, Experiment, Formal analysis, Writing – review & editing. **Meng Zhou:** Resources, Theoretical analysis, Formal analysis. **Yi Zhang:** Formal analysis, Writing – review & editing. **Deye Xu:** Experiment, Formal analysis. **Zhiyang Zhang:** Data curation, Formal analysis. **Xianhua Zheng:** Data curation, Formal analysis. **De Li:** Data curation, Formal analysis. **Xu Li:** Investigation, Formal analysis. **Baohong Tian:** Theoretical analysis, Supervision. **Yanlin Jia:** Formal analysis. **Yong Liu:** Visualization. **Alex A. Volinsky:** Writing – review & editing. **Ekaterina S. Marchenko:** Writing – review & editing.

Declaration of competing interest

The authors declare that they have no known competing financial interests or personal relationships that could have appeared to influence the work reported in this paper.

Data availability

No data was used for the research described in the article.

Acknowledgments

This work was supported by the National Natural Science Foundation of China (52071134, 92060102, 52101083), Outstanding Talents Innovation Fund of Henan Province (ZYQR201912164), the Program for Innovative Research Team at the University of the Henan Province (22IRTSTHN001), China Postdoctoral Science Foundation (2020M682316, 2021T140779).

References

[1] J.K. Li, Z.W. Zhang, W.H. Xu, Y.Q. Yang, P.J. Xue, Q. Teng, C. Cai, W. Li, Q.S. Wei, Hot isostatic pressing of Cu-15Ni-8Sn alloy with suppressed Sn macro-segregation and enhanced mechanical properties, Mater. Sci. Eng., A 855 (2022), 143886, https://doi.org/10.1016/j.msea.2022.143866.

[2] S. Li, M. Fang, Z. Xiao, X. Meng, Q. Lei, Y. Jia, Effect of Cr addition on corrosion behavior of cupronickel alloy in 3.5 wt% NaCl solution, J. Mater. Res. Technol. 22 (2023) 2222–2238, https://doi.org/10.1016/j.jmrt.2022.12.079.

[3] M.Z. Ma, Z. Xiao, X.P. Meng, Z. Li, S. Gong, J. Dai, H.Y. Jiang, Y.B. Jiang, Q. Lei, H. G. Wei, Effects of trace calcium and strontium on microstructure and properties of Cu-Cr alloys, J. Mater. Sci. Technol. 112 (2022) 11–23, https://doi.org/10.1016/j.jmst.2021.08.080.

[4] Y.D. Wang, M. Liu, B.H. Yua, L.H. Wu, P. Xue, D.R. Ni, Z.Y. Ma, Enhanced combination of mechanical properties and electrical conductivity of a hard state Cu-Cr-Zr alloy via one-step friction stir processing, J. Mater. Process. Technol. 288 (2021), 116880, https://doi.org/10.1016/j.jmatprotec.2020.116880.

[5] Y. Ding, Z. Xiao, M. Fang, S. Gong, J. Dai, Microstructure and mechanical properties of multi-scale α-Fe reinforced Cu-Fe composite produced by vacuum suction casting, Mater. Sci. Eng., A 864 (2023), 144603, https://doi.org/10.1016/j.msea.2023.144603.

[6] B.M. Luo, D.X. Li, C. Zhao, Z. Wang, Z.Q. Luo, W.W. Zhang, A low Sn content Cu-Ni-Sn alloy with high strength and good ductility, Mater. Sci. Eng., A 746 (2019) 154–161, https://doi.org/10.1016/j.msea.2018.12.120.

[7] S.R. Zhang, J.Q. Shi, L. Zhao, L.G. Chen, Z.Z. Lin, G.P. Tang, P.J. Shi, T.X. Zheng, Y. F. Guo, Q. Li, Z. Shen, B. Ding, Y.B. Zhong, Influence of as-cast structure refinement on heritability of mechanical properties for Cu-15Ni-8Sn alloys, Mater. Lett. 328 (2022), 133097, https://doi.org/10.1016/j.matlet.2022.133097.

[8] W.J. Liu, X. Chen, T.H. Ahmad, C.Y. Zhou, X.P. Xiao, H. Wang, B. Yang, Microstructures and mechanical properties of Cu-Ti alloys with ultrahigh strength and high ductility by thermo-mechanical treatment, Mater. Sci. Eng., A 835 (2022), 142672, https://doi.org/10.1016/j.msea.2022.142672.

[9] B. Rouxel, C. Cayron, J.L. Bornand, P. Sanders, R.E. Logé, Micro-addition of Fe in highly alloyed Cu-Ti alloys to improve both formability and strength, Mater. Des. 213 (2022), 110340, https://doi.org/10.1016/j.matdes.2021.110340.

[10] L. Zhu, Z.P. Zhong, H. Yang, C.H. Wang, Comparison study of Cu-Fe-Ti and Co-Fe-Ti oxide catalysts for selective catalytic reduction of NO with NH3 at low temperature, J. Colloid Interface Sci. 478 (2016) 11–21, https://doi.org/10.1016/j.jcis.2016.05.052.

[11] H.Y. Yang, Y.Q. Bu, J.M. Wu, Y.T. Fang, J.B. Liu, L.Y. Huang, H. T Wang, High strength, high conductivity and good softening resistance Cu-Fe-Ti alloy, J. Alloys Compd. 925 (2022), 166595, https://doi.org/10.1016/j.jallcom.2022.166595.

[12] A. Agrawal, R.K. Dube, Methods of fabricating Cu-Al-Ni shape memory alloys, J. Alloys Compd. 750 (2018) 235–247, https://doi.org/10.1016/j.jallcom.2018.03.390.

[13] S.X. Zhang, L. Wu, T. Gu, Y.C. Shi, X.L. Tian, H.Q. Li, H. Hou, Y.H. Zhao, Effect of microstructure on the mechanical properties of ultrafinegrained Cu-Al-Ni alloys processed by deformation and annealing, J. Alloys Compd. 923 (2022), 166413, https://doi.org/10.1016/j.jallcom.2022.166413.

[14] X.Q. Lv, Z.M. Liu, T. Lei, Q. Li, F. Zhao, K. Peng, Y.K. Ren, S.Z. Lu, B.Z. Nong, Microstructure and properties of Cu-Cr-Nb alloy powder prepared by argon gas atomization, Adv. Powder Technol. 30 (2019) 2464–2472, https://doi.org/10.1016/j.apt.2019.07.013.

[15] M. Zhang, J.C. Gibeling, Understanding creep mechanisms of a Cu-Cr-Nb alloy by testing under constant structure conditions, Scripta Mater. 190 (2021) 131–135, https://doi.org/10.1016/j.scriptamat.2020.08.036.

[16] Y. Ouyang, X.P. Gan, S.Z. Zhang, Z. Li, K.C. Zhou, Y.X. Jiang, X.W. Zhang, Age-hardening behavior and microstructure of Cu-15Ni-8Sn-0.3 Nb alloy prepared by powder metallurgy and hot extrusion, Trans. Nonferrous Metals Soc. China 27 (2017) 1947–1955, https://doi.org/10.1016/S1003-6326(17)60219-X.

[17] J. Liu, X.H. Wang, J. Chen, J.T. Liu, The effect of cold rolling on age hardening of Cu-3Ti-3Ni-0.5Si alloy, J. Alloys Compd. 797 (2019) 370–379, https://doi.org/10.1016/j.jallcom.2019.05.091.

[18] J.J. Cheng, M.C. Mao, X.P. Gan, Q. Lei, Z. Li, K.C. Zhou, Microstructures, mechanical properties, and grease-lubricated sliding wear behavior of Cu-15Ni-8Sn-0.8Nb alloy with high strength and toughness, Friction 9 (5) (2020) 1061–1076, https://doi.org/10.1007/s40544-020-0399-7.

[19] C.J. Guo, J.S. Chen, X.P. Xiao, H. Huang, W.J. Wang, B. Yang, The effect of Co addition on the modulated structure coarsening and discontinuous precipitation growth kinetics of Cu-15Ni-8Sn alloy, J. Alloys Compd. 835 (2020), 155275, https://doi.org/10.1016/j.jallcom.2020.155275.

[20] Z.K. Huang, R.H. Shi, X.Y. Xiao, H.D. Fu, Q. Chen, J.X. Xie, Mechanism investigation on high-performance Cu-Cr-Ti alloy via integrated computational materials engineering, Mater. Today Commun. 27 (2021), 102378, https://doi.org/10.1016/j.mtcomm.2021.102378.

[21] B.J. Wang, Y. Zhang, B.H. Tian, J.C. An, A.A. Volinsky, H. Sun, Y. Liu, K.X. Song, Effects of Ce addition on the Cu-Mg-Fe alloy hot deformation behavior, Vacuum 155 (2018) 594–603, https:/doi.org/10.1016/j.vacuum.2018.06.006.

[22] L. Si, L. Zhou, X. Zhou, S.H. Li, L.N. Shen, Q.Y. Dong, Microstructure and property of Cu-2.7Ti-0.15Mg-0.1Ce-0.1Zr alloy treated with a combined aging process, Mater. Sci. Eng., A 650 (2016) 345–353, https://doi.org/10.1016/j.msea.2015.10.062.

[23] S.L. Tang, M. Zhou, X. Li, Y. Zhang, D.Y. Xu, Z.Y. Zhang, B.H. Tian, Y.L. Jia, Y. Liu, A.A. Volinsky, E.S. Marchenko, Microstructure and hot deformation behavior of the Cu-1Ni-0.9Sn-0.5Ti-0.3Cr alloy, Mater. Today Commun. 31 (2022), 102266, https://doi.org/10.1016/j.mtcomm.2022.103771.

[24] K.D. Ukabhai, U.A. Curle, N.D.E. Masia, M. Smit, I.A. Mwamba, S. Norgren, C. Öhman-Mägi, N.G. Hashe, L.A. Cornish, formation of Ti2Cu in Ti-Cu alloys, J. Phase Equilibria Diffus. 43 (2022) 332–344, https://doi.org/10.1007/s11669-022-00964-7.

[25] Q. Lei, Z. Xiao, W.P. Hu, B. Derby, Z. Li, Phase transformation behaviors and properties of a high strength Cu-Ni-Si alloy, Mater. Sci. Eng., A 697 (2017) 37–47, https://doi.org/10.1016/j.msea.2017.05.001.

[26] Y.J. Ban, Y.F. Geng, J.R. Hou, Y. Zhang, M. Zhou, Y.L. Jia, B.H. Tian, Y. Liu, X. Li, A.A. Volinsky, Properties and precipitates of the high strength and electrical conductivity Cu-Ni-Co-Si-Cr alloy, J. Mater. Sci. Technol. 93 (2021) 1–6, https://doi.org/10.1016/j.jmst.2021.03.049.

[27] S.L. Fu, P. Liu, X.H. Chen, H.L. Zhou, F.C. Ma, W. Li, K. Zhang, Effect of aging process on the microstructure and properties of Cu-Cr-Ti alloy, Mater. Sci. Eng., A 802 (2021), 140598, https://doi.org/10.1016/j.msea.2020.140598.

[28] J. Dai, M.Z. Ma, Z. Xiao, X.P. Meng, G. Sun, T.Y. Zhang, T. Zhou, L.H. Li, Y.X. Zhu, Effect of trace silicon addition on microstructure and properties of a Cu-0.26Cr-0.14Mg alloy, Mater. Sci. Eng., A 833 (2022), 142511, https://doi.org/10.1016/j.msea.2021.142511.

[29] M.Z. Ma, Z. Li, Z. Xiao, Y.L. Jia, X.P. Meng, Y.B. Jiang, Y. Hu, Microstructure and properties of Cu-Ni-Co-Si-Cr-Mg alloys with different Si contents after multi-step

thermo-mechanical treatment, Mater. Sci. Eng., A 850 (2022), 143532, https://doi.org/10.1016/j.msea.2022.143532.
[30] J.Y. Cheng, B.B. Tang, F.X. Yu, B. Shen, Evaluation of nanoscale precipitates in a Cu-Ni-Si-Cr alloy during aging, J. Alloys Compd. 614 (2014) 189–195, https://doi.org/10.1016/j.jallcom.2014.06.089.
[31] W.Y. Wang, Z. Xiao, Q. Lei, H. Meng, Q.H. Guo, Y.H. Yang, Z. Li, A multiphase strengthened Cu-Nb-Si alloy with high strength and high conductivity, Mater. Char. 182 (2021), 111565, https://doi.org/10.1016/j.matchar.2021.111565.
[32] Y.K. Ren, X.Q. Lü, Z.M. Liu, B. Wei, T. Lei, Q. Li, X.B. Ji, W.T. Deng, Y.K. Ai, Microstructure and properties of Cu-2Cr-1Nb alloy fabricated by spark plasma sintering, T. Nonferr. Metal. Soc. 32 (2022) 2276–2289, https://doi.org/10.1016/S1003-6326(22)65947-8.
[33] J. Li, G.J. Huang, X.J. Mi, L.J. Peng, H.F. Xie, Y.L. Kang, Microstructure evolution and properties of a quaternary Cu-Ni-Co-Si alloy with high strength and conductivity, Mater. Sci. Eng., A 766 (2019), 138390, https://doi.org/10.1016/j.msea.2019.138390.
[34] C. Zhao, Z. Wang, D.X. Li, D.Q. Pan, B.M. Lou, Z.Q. Luo, W.W. Zhang, Optimization of strength and ductility in an as-extruded Cu-15Ni-8Sn alloy by the additions of Si and Ti, J. Alloys Compd. 823 (2020), 153759, https://doi.org/10.1016/j.jallcom.2020.153759.
[35] Z. Shen, Z.G. Lin, P.J. Shi, J.L. Zhu, T.X. Zheng, B. Ding, Y.F. Guo, Y.B. Zhong, Enhanced electrical, mechanical and tribological properties of Cu-Cr-Zr alloys by continuous extrusion forming and subsequent aging treatment, J. Mater. Sci. Technol. 110 (2022) 187–197, https://doi.org/10.1016/j.jmst.2021.10.012.
[36] Y.F. Geng, Y.J. Ban, X. Li, Y. Zhang, Y.L. Jia, B.H. Tian, M. Zhou, Y. Liu, A. A. Volinsky, K.X. Song, S.L. Tang, Excellent mechanical properties and high electrical conductivity of Cu-Co-Si-Ti alloy due to multiple strengthening, Mater. Sci. Eng., A 821 (2021), 141639, https://doi.org/10.1016/j.msea.2021.141639.
[37] D. Jorge-Badiola, A. Iza-Mendia, I. Gutiérrez, Study by EBSD of the development of the substructure in a hot deformed 304 stainless steel, Mater. Sci. Eng., A 394 (2005) 445–454, https://doi.org/10.1016/j.msea.2004.11.049.
[38] Y.F. Geng, Y. Zhang, K.X. Song, Y.L. Jia, X. Li, H. Stock, H.L. Zhou, B.H. Tian, Y. Liu, A.A. Volinsky, X.H. Zhang, P. Liu, X.H. Chen, Effect of Ce addition on microstructure evolution and precipitation in Cu-Co-Si-Ti alloy during hot deformation, J. Alloys Compd. 842 (2020), 155666, https://doi.org/10.1016/j.jallcom.2020.155666.
[39] Y.J. Ban, Y. Zhang, B.H. Tian, K.X. Song, M. Zhou, X.H. Zhang, Y.L. Jia, X. Li, Y. F. Geng, Y. Liu, A.A. Volinsky, EBSD analysis of hot deformation behavior of Cu-Ni-Co-Si-Cr alloy, Mater. Char. 169 (2020), 110656, https://doi.org/10.1016/j.matchar.2020.110656.
[40] A.S.H. Kabir, M. Sanjari, J. Su, I.-H. Jung, S. Yue, Effect of strain-induced precipitation on dynamic recrystallization in Mg-Al-Sn alloys, Mater. Sci. Eng., A 616 (2014) 252–259, https://doi.org/10.1016/j.msea.2014.08.032.
[41] Y.L. Jia, Y. Pang, J. Yi, Q. Lei, Z. Li, Z. Xiao, Effects of pre-aging on microstructure and properties of Cu-Ni-Si alloys, J. Alloys Compd. 942 (2023), 169033, https://doi.org/10.1016/j.jallcom.2023.169033.
[42] S. Nagarjuna, M. Srinivas, Elevated temperature tensile behaviour of a Cu-4.5Ti alloy, Mater. Sci. Eng., A 406 (2005) 186–194, https://doi.org/10.1016/j.msea.2005.06.064.
[43] S. Nagarjuna, K. Balasubramanian, Effect of prior cold work on mechanical properties, electrical conductivity and microstructure of aged Cu-Ti alloys, J. Mater. Sci. 34 (1999) 2929–2942, https://doi.org/10.1023/A:1004603906359.
[44] X.L. Zhuang, S. Antonov, L.F. Li, Q. Feng, Effect of alloying elements on the coarsening rate of γ' precipitates in multi-component CoNi-based superalloys with high Cr content, Scripta Mater. 202 (2021), 114004, https://doi.org/10.1016/j.scriptamat.2021.114004.
[45] W.J. Liu, J. Li, X. Chen, M.H. Ji, X.P. Xiao, H. Wang, B. Yang, Effect of vanadium on the microstructure and kinetics of discontinuous precipitation in Cu-3.2Ti-0.2Fe alloy, J. Mater. Res. Technol. 14 (2021) 121–136, https://doi.org/10.1016/j.jmrt.2021.06.045.
[46] Y.K. Wu, Y. Li, J.Y. Lu, S. Tan, F. Jiang, J. Sun, Effects of pre-deformation on precipitation behaviors and properties in Cu-Ni-Si-Cr alloy, Mater. Sci. Eng., A 742 (2019) 501–507, https:/doi.org/10.1016/j.msea.2018.11.045.
[47] J.Y. He, H. Wang, H.L. Huang, X.D. Xu, M.W. Chen, Y. Wu, X.J. Liu, T.G. Nieh, K. An, Z.P. Lu, A precipitation hardened high-entropy alloy with outstanding tensile properties, Acta Mater. 102 (2016) 187–196, https:/doi.org/10.1016/j.actamat.2015.08.076.
[48] M. Gholami, J. Vesely, I. Altenberger, H.A. Kuhn, M. Janecek, M. Wollmann, L. Wagner, Effects of microstructure on mechanical properties of CuNiSi alloys, J. Alloys Compd. 696 (2017) 201–212, https://doi.org/10.1016/j.jallcom.2016.11.233.
[49] N. Hansen, Hall-Petch relation and boundary strengthening, Scripta Mater. 51 (2004) 801–806, https://doi.org/10.1016/j.scriptamat.2004.06.002.
[50] Z.W. Wang, W.J. Lu, H. Zhao, C.H. Liebscher, J.Y. He, D. Ponge, D. Raabe, Z.M. Li, Ultra-strong lightweight compositionally complex steels via dual-nanoprecipitation, Sci. Adv. 6 (2020) 1–7, https://doi.org/10.1126/sciadv.aba9543.
[51] Y.K. Wu, Y. Li, J.Y. Lu, S. Tan, F. Jiang, J. Sun, Correlations between microstructures and properties of Cu-Ni-Si-Cr alloy, Mater. Sci. Eng. 731 (2018) 403–412, https://doi.org/10.1016/j.msea.2018.06.075.
[52] A. Matthiessen, C. Vogt, On the influence of temperature on the electric conducting-power of alloys, Phil. Trans. Roy. Soc. Lond. 154 (1864) 167–200, https://doi.org/10.1098/rspl.1862.0142.
[53] W. Zeng, J.W. Xie, D.S. Zhou, Z.Q. Fu, D.L. Zhang, E.J. Lavernia, Bulk Cu-NbC nanocomposites with high strength and high electrical conductivity, J. Alloys Compd. 745 (2018) 55–62, https://doi.org/10.1016/j.jallcom.2018.02.215.
[54] L. Qian, Electrical resistivity of fully-relaxed grain boundaries in nanocrystalline Cu, Scripta Mater. 50 (2004) 1407–1411, https://doi.org/10.1016/j.scriptamat.2004.02.026.
[55] Z.R. Zeng, Y.M. Zhu, R.L. Liu, S.W. Xu, C.H.J. Davies, J.F. Nie, N. Birbilis, Achieving exceptionally high strength in Mg-3Al-1Zn-0.3Mn extrusions via suppressing intergranular deformation, Acta Mater. 160 (2018) 97–108, https://doi.org/10.1016/j.actamat.2018.08.045.